Incremental pressure correction method for subsonic compressible flows

Jerome Jansen[a,b], Stéphane Glockner[a,b,*], Deewakar Sharma[a,b], Arnaud Erriguible[a,b]

[a] *Univ. Bordeaux, CNRS, Bordeaux INP, I2M, UMR 5295, F-33400, Talence, France ,*
[b] *Arts et Metiers Institute of Technology, CNRS, Bordeaux INP, Hesam Universite, I2M, UMR 5295, F-33400 Talence, France ,*

Abstract

We present an original method for the treatment of pressure-velocity coupling in the context of subsonic compressible flows. The proposed method considers an elliptic equation for the time increment of the pressure and can be seen as the extension of the widely used incremental pressure correction method for incompressible flows to compressible flows. The compressible Navier–Stokes equations are coupled with the energy conservation equation and any fluid equation of state. After deriving the method, spatial and temporal second-order convergence for velocity, pressure, temperature, and density is measured on several verification test cases, whether manufactured or not, with Mach numbers up to 0.6. The method is subsequently applied to steady and unsteady high-gradient temperature and density flows, *i.e.* beyond the Boussinesq approximation, as well as thermoacoustic wave propagation problems.

Keywords: compressible flows, pressure-based method, time-splitting, incremental pressure correction method, projection method, subsonic, low Mach, free convection, thermoacoustic wave

Code availability. The implementation of the proposed method and all the test cases presented in this paper are available in the Notus CFD repository https://notus-cfd.org/ (code v0.6.0).

*Corresponding author.
Email addresses: jerome.jansen@u-bordeaux.fr (Jerome Jansen), stephane.glockner@bordeaux-inp.fr (Stéphane Glockner), deewakar.edu@gmail.com (Deewakar Sharma), arnaud.erriguible@bordeaux-inp.fr (Arnaud Erriguible)

Contents

1. Introduction

The resolution of pressure-velocity coupling for solving incompressible and compressible fluid problems has been a subject of extensive research. The state-of-art methods, beyond their ability to answer the posed problem, have several aspects that need to be carefully addressed in order to define their applicability and robustness for high fidelity simulations, such as spatial and temporal convergence orders, multiphase flows with high density jump, outflow boundary conditions, CPU time, parallel efficiency, etc.

The common classification for solving compressible flow problems divides methods into density-based and pressure-based. Both use the momentum equation to calculate velocity field and primarily differ in their approach to calculate the density and the pressure fields. Coming from the supersonic flow community [1, 2, 3, 4], density-based methods access the density by solving the mass conservation equation and use the equation of state for computing the pressure field. Though the method has been mainly designed for high Mach flows, several authors [5, 6, 7, 8, 9] have extended its utility to Ma less than 0.3 problems by addressing the inaccuracy which arise in these cases. Pressure-based methods, initially developed within the incompressible flow community [10, 11, 12] have been extended to low-mach or weakly compressible flows [13, 14, 15, 16, 17, 18, 19] and all-speed flows [20, 21, 22, 23, 24, 25, 26]. They are characterized by solving implicitly a derived pressure equation from a combination of momentum and mass conservation. For problems with variable density, density field can be computed from an equation of state knowing the resolved pressure field. The proposed method in this article belongs to the pressure-based category of methods.

For incompressible flows, pressure correction methods are commonly employed. These methods involve initially predicting the velocity field by solving the conservation of momentum equation, followed by a correction step to obtain a solenoidal velocity field by solving a pressure equation. A pioneering method, still widely used, was developed by Chorin [10]. It involves solving the prediction step by neglecting the pressure gradient in the momentum equation, followed by solving a Laplacian on the pressure, with the gradient used to ensure a divergence-free velocity field. While applicable to both single-phase and two-phase flows, this method is known to suffer from a low temporal convergence order. The Chorin method was later improved upon by Goda [27] and subsequently by Timmermans et al. [28], introducing the incremental pressure correction method and the rotational incremental pressure correction method, respectively. Unlike Chorin's method, both Goda's and Timmermans' methods incorporate the pressure gradient in the prediction stage. The unknown resolved variable in the correction stage is the time increment of the pressure. The precise mathematical analysis of these schemes has been carried out in the work of Guermond et al. [29]. An important parameter to characterize a resolution methodology is the order of convergence, both in space and time. In the aforementioned methods of Chorin [10] and Goda [27], the boundary condition on the pressure or its increment creates an artificial boundary layer that does not compromise the spatial precision of the discretization. However, there are significant differences in the order of temporal convergence among the original method and its variants. With Dirichlet boundary conditions applied on the velocity, the standard non-incremental method by Chorin [10] converges in time at order 1 for velocity and $1/2$ for pressure. In comparison, the incremental standard method by Goda [27] converges at orders 2 and 1 for velocity and pressure, respectively, while the incremental rotational method by Timmermans et al. [28] — reducing the articificial boundary layer — converges at orders 2 and $3/2$ for velocity and pressure, respectively.

In the context of compressible subsonic flows and pressure-based methods, the full form of the mass conservation equation and thermodynamic effects make the resolution of the pressure-velocity coupling even more complex. For more than two decades, several authors have proposed methods based on an elliptic equation for the pressure [30, 24, 25, 31, 32, 26, 17, 33, 34, 35] that can be considered as non incremental pressure correction methods for compressible flows. They have been successfully applied to single as well as multiphase flows. To the best of the authors' knowledge, a general incremental pressure correction method has not yet been proposed.

Further, though some works can be found where the authors have performed spatial convergence studies for compressible flows using manufactured or exact solutions [14, 36, 31, 37, 38, 39, 19], very few have presented temporal convergence studies [14, 35, 18, 19]. Among the limited work to the author's knowledge, Moureau et al. [35] and Cang and Wang [19] only perform a temporal convergence study on the linear acoustic propagation problem with periodic boundary conditions to exibit second-order and first-order temporal accuracy of their methods, respectively. Hennink et al. [18] proposed a more general manufactured solution of the compressible Navier-Stokes equation coupled with enthalpy equation. On constant- and variable-density solutions with Dirichlet and Neumann boundary conditions, they observed a full second-order temporal accuracy of their proposed pressure-based discontinuous Galerkin method.

This article proposes an incremental pressure correction method for general subsonic compressible flows (IPCMSF). While the traditional approach for constructing the correction step in this class of methods for incompressible flows relies on the null divergence property of the velocity field, our method for compressible flows involves leveraging the pressure equation [40], which includes a divergence term of the velocity. Furthermore, our proposed method couples the Navier-Stokes equation with the energy equation under its c_p formulation and permits using any equation of state for density. The key feature of this work has been to achieve second-order spatial and temporal accuracy, for velocity, pressure, temperature and density. The verification process systematically present temporal convergence studies for different benchmarks of increasing complexity, from 0D test case to manufactured 2D solution with variable material properties and Dirichlet boundary conditions for velocity and temperature. The current work focuses only on single-phase flow with Dirichlet boundary conditions on velocity, while outlet/open boundary conditions and considerations for multiphase flow are beyond the scope of this article and will be covered up in the future work.

The article is structured as follows: Section 2 presents a review of the governing equations for compressible flow in primitive variables; In Section 3, we propose the pressure increment correction method applied to subsonic compressible flows; Section 4 focuses on the numerical framework, employing implicit discretization of the equations using the second-order finite volume method with first and second-order temporal orders; Section 5 illustrates various test cases for verification of the developed method covering (a) isentropic injection and linear acoustic pulse propagation test cases and (b) a manufactured solution tailored to low to Mach numbers close to 0.6. These cases are utilized to compute spatial and temporal convergence orders; Section 6 presents numerical applications in 2D stationary and unsteady natural convection outside the Boussinesq approximation, focusing on various ranges of subsonic Mach numbers. Thermoacoustic wave propagation in perfect gas and supercritial carbon dioxide are also studied; Lastly, conclusions and perspectives are provided in Section 7.

2. Governing equations

2.1. Classical formulation of a compressible flow

The governing equations of a compressible flow for a Newtonian fluid expresses the conservation of mass, momentum and energy in c_p formulation, respectively

$$\frac{\partial \rho}{\partial t} + \boldsymbol{\nabla} \cdot (\rho \boldsymbol{v}) = 0\,, \tag{1a}$$

$$\rho \left(\frac{\partial \boldsymbol{v}}{\partial t} + (\boldsymbol{v} \cdot \boldsymbol{\nabla})\, \boldsymbol{v} \right) = -\boldsymbol{\nabla} p + \boldsymbol{\nabla} \cdot (\mu \dot{\boldsymbol{\gamma}}) - \frac{2}{3} \boldsymbol{\nabla} \left(\mu \boldsymbol{\nabla} \cdot \boldsymbol{v} \right) + \rho \boldsymbol{g}\,, \tag{1b}$$

$$\rho c_p \left(\frac{\partial T}{\partial t} + \boldsymbol{v} \cdot \boldsymbol{\nabla} T \right) = T \beta_p \left(\frac{\partial p}{\partial t} + \boldsymbol{v} \cdot \boldsymbol{\nabla} p \right) + \boldsymbol{\nabla} \cdot (\lambda \boldsymbol{\nabla} T) + \Phi_d(\boldsymbol{v})\,. \tag{1c}$$

These conservation equations are written in terms of primitive variables, with $T(\boldsymbol{x}, t)$ the temperature field, $p(\boldsymbol{x}, t)$ the pressure field, $\boldsymbol{v}(\boldsymbol{x}, t)$ the velocity field, and $\rho(\boldsymbol{x}, t)$ the density field. In (1b), the strain rate tensor is defined as $\dot{\boldsymbol{\gamma}} = \boldsymbol{\nabla} \boldsymbol{v} + \boldsymbol{\nabla} \boldsymbol{v}^T$, μ is the dynamic viscosity of the fluid, $\boldsymbol{g}$ is the gravitational acceleration, and we consider the Stokes' hypothesis for the second coefficient of viscosity $\lambda_\mu = -\frac{2}{3}\mu$. In (1c), c_p denotes the specific heat capacity, $\beta_p = -\frac{1}{\rho} \left.\frac{\partial \rho}{\partial T}\right|_p$ is the isobaric thermal expansion coefficient, λ is the thermal conductivity, and Φ_d is the viscous dissipation rate of energy defined as

$$\Phi_d = -\frac{2\mu}{3} \left(\boldsymbol{\nabla} \cdot \boldsymbol{v} \right)^2 + \frac{\mu}{2} \dot{\boldsymbol{\gamma}} : \dot{\boldsymbol{\gamma}}\,. \tag{2}$$

For the sake of generalization, we have introduced Φ_d within the equations of the article, but this term will be ignored in all the simulations from Section 5.

To close the system of equations introduced above, specifying the necessary initial and boundary conditions to prevent the problem being ill-posed is required along with an equation of state (EoS) for density in addition to certain material properties x, *e.g.* isothermal compressibility, thermal expansion, speed of sound or heat capacity

$$x = \mathrm{EoS}(T, p)\,. \tag{3}$$

2.2. Derivation of the pressure-energy equation

An alternative form of the energy equation is derived by expanding the material derivative of pressure as a function of temperature and density

$$\frac{\mathrm{D}p}{\mathrm{D}t} = \left.\frac{\partial p}{\partial \rho}\right|_T \frac{\mathrm{D}\rho}{\mathrm{D}t} + \left.\frac{\partial p}{\partial T}\right|_\rho \frac{\mathrm{D}T}{\mathrm{D}t}\,, \tag{4}$$

with the material derivative of any scalar and vector fields $*$ being defined as

$$\frac{\mathrm{D}*}{\mathrm{D}t} = \frac{\partial *}{\partial t} + \boldsymbol{v}\cdot\boldsymbol{\nabla} *\,. \tag{5}$$

Using mass conservation (1a) and introducing the respective thermodynamic coefficients of isobaric thermal expansion and isothermal compressibility, defined as follows

$$\beta_p = -\frac{1}{\rho}\left.\frac{\partial \rho}{\partial T}\right|_P \quad \text{and} \quad \chi_T = \frac{1}{\rho}\left.\frac{\partial \rho}{\partial p}\right|_T\,, \tag{6}$$

equation (4) reads

$$\frac{\mathrm{D}p}{\mathrm{D}t} = -\frac{1}{\chi_T}\boldsymbol{\nabla}\cdot\boldsymbol{v} + \frac{\beta_p}{\chi_T}\frac{\mathrm{D}T}{\mathrm{D}t}\,. \tag{7}$$

By applying the conservation of energy (1c) in conjunction with thermodynamic relations followed by few algebraic manipulations, we obtain

$$\frac{\mathrm{D}p}{\mathrm{D}t} = -\rho c^2\boldsymbol{\nabla}\cdot\boldsymbol{v} + \frac{\beta_p c^2}{c_p}\left(\boldsymbol{\nabla}\cdot(\lambda\boldsymbol{\nabla}T) + \Phi_d\right)\,, \tag{8}$$

with c denoting the speed of sound. A more descriptive derivation of pressure-energy equation is provided in Appendix A.

The pressure-energy conservation equation for incompressible flow reduces to $\boldsymbol{\nabla}\cdot\boldsymbol{v}=0$ ($c\to\infty$ and $\beta_p=0$), *i.e.* $\mathrm{D}\rho/\mathrm{D}t=0$, which is consistent with the incompressibility limit. While several authors have already used a similar form of the conservation of energy expressed in terms of pressure (8) [20, 41, 35, 30, 42, 43, 44, 40, 17, 33, 45], the originality of the proposed approach is to use it to derive the incremental pressure correction method. In addition, the proposed modelling of a compressible flow (1) (21) (8) as well as our method as presented in Section 3 make no assumptions about the type of fluid thereby making it feasible to cover a wide range of fluids using any appropriate EoS.

3. The incremental pressure correction method

3.1. Derivation of the equation for the time pressure increment

An incremental pressure correction approach for compressible flow requires the development and the resolution of an equation specifically dedicated to the pressure increment, denoted by φ. Following the original incremental pressure correction method applied for incompressible flows [27], we write the pressure at next iteration as $p^{n+1}=p^n+\varphi$.

Since density varies in compressible flows, the first step of the current method seeks to have an estimate of the density field, ρ^{n+1}, denoted by $\rho^\dagger$. This is obtained through extrapolation at the desired order, *e.g.* for first-order in time $\rho^\dagger=\rho^n$ and for second-order in time with constant time step as $\rho^\dagger=2\rho^n-\rho^{n-1}$. Henceforth, any variable $x^\dagger$ will be an estimate of x at the order of the chosen temporal scheme.

A predicted velocity, denoted by $\boldsymbol{v}^*$, is obtained by solving the momentum equation considering the pressure gradient at time t^n

$$\rho^\dagger\left(\frac{a\boldsymbol{v}^*+b\boldsymbol{v}^n+c\boldsymbol{v}^{n-1}}{\Delta t}+\boldsymbol{\nabla}\cdot\left(\boldsymbol{v}^\dagger\otimes\boldsymbol{v}^*\right)-\boldsymbol{v}^*\boldsymbol{\nabla}\cdot\boldsymbol{v}^\dagger\right)=-\boldsymbol{\nabla}p^n+\boldsymbol{\nabla}\cdot\left(\mu^\dagger\dot{\boldsymbol{\gamma}}^*\right)-\frac{2}{3}\boldsymbol{\nabla}\left(\mu^\dagger\boldsymbol{\nabla}\cdot\boldsymbol{v}^*\right)+\rho^\dagger\boldsymbol{g}\,, \tag{9}$$

with a,b,c denoting the time discretization coefficients of first-order Euler backward scheme ($a=1$, $b=-1$, $c=0$) or second-order Backward Differentiation Formula ($a=3/2$, $b=-2$, $c=1/2$). Equation (9) is written in its fully implicit form, but it could also be written in semi- or fully-explicit form depending on the scales of a given problem.

Following Goda's classical approach, we write the pressure increment equation by taking the difference between (1b) evaluated at time t^{n+1} and (9), while neglecting the nonlinear and the divergence terms of the stress tensor, as

$$\boldsymbol{v}^{n+1}-\boldsymbol{v}^*=-k_\varphi^\dagger\boldsymbol{\nabla}\varphi\,, \tag{10}$$

with $k_\varphi^\dagger=\frac{\Delta t}{a\rho^\dagger}$. Taking the divergence of (10), it reads

$$\boldsymbol{\nabla}\cdot\boldsymbol{v}^{n+1}-\boldsymbol{\nabla}\cdot\boldsymbol{v}^*=-\boldsymbol{\nabla}\cdot\left(k_\varphi^\dagger\boldsymbol{\nabla}\varphi\right)\,. \tag{11}$$

Compared to incompressible flows, where we have a divergence-free velocity, we aim to replace the velocity divergence term in compressible flows $\boldsymbol{\nabla}\cdot\boldsymbol{v}^{n+1}$ in (11) by the following relation coming from the discretized pressure-energy equation (8)

$$\frac{ap^{n+1}+bp^n+cp^{n-1}}{\Delta t}+\boldsymbol{v}^\dagger\cdot\boldsymbol{\nabla}p^\dagger=-(\rho c^2)^\dagger\boldsymbol{\nabla}\cdot\boldsymbol{v}^{n+1}+\left(\frac{\beta_p c^2}{c_p}\right)^\dagger\left(\boldsymbol{\nabla}\cdot(\lambda^\dagger\boldsymbol{\nabla}T^\dagger)+\Phi_d^\dagger\right)\,. \tag{12}$$

By rearranging the terms and by expressing φ, we obtain

$$\boldsymbol{\nabla}\cdot\boldsymbol{v}^{n+1}=\left(-\frac{a\varphi}{\Delta t}-\frac{(a+b)p^n+cp^{n-1}}{\Delta t}-\boldsymbol{v}^\dagger\cdot\boldsymbol{\nabla}p^\dagger+\left(\frac{\beta_p c^2}{c_p}\right)^\dagger\left(\boldsymbol{\nabla}\cdot(\lambda^\dagger\boldsymbol{\nabla}T^\dagger)+\Phi_d^\dagger\right)\right)\Big/(\rho c^2)^\dagger\,. \tag{13}$$

Finally, combining (13) and (11), we obtain the following elliptic equation with variable coefficients for the pressure increment

$$\frac{a\varphi}{(\rho c^2)^\dagger\Delta t}-\boldsymbol{\nabla}\cdot\left(k_\varphi^\dagger\boldsymbol{\nabla}\varphi\right)=-\boldsymbol{\nabla}\cdot\boldsymbol{v}^*+\dot{S}_\varphi^\dagger\,, \tag{14}$$

with the compressible pressure increment source term given by,

$$\dot{S}_\varphi^\dagger=\left(\left(\frac{\beta_p c^2}{c_p}\right)^\dagger\left(\boldsymbol{\nabla}\cdot(\lambda^\dagger\boldsymbol{\nabla}T^\dagger)+\Phi_d^\dagger\right)-\boldsymbol{v}^\dagger\cdot\boldsymbol{\nabla}p^\dagger-\frac{(a+b)p^n+cp^{n-1}}{\Delta t}\right)\Big/(\rho c^2)^\dagger\,. \tag{15}$$

It is worth highlighting that when $c\to\infty$ and $\beta_p=0$, the pressure correction equation (14) is reduced to that of the incompressible case. Thus, the proposed method is valid in the limit of incompressible flows. This has been numerically verified. As the results are strictly identical to those given by the incremental pressure correction method for incompressible flows, they are not shown in this paper in order to better concentrate on various subsonic flows.

3.2. Full semi-implicit system of equation

This section sums up the proposed incremental pressure correction method for compressible flow. Firstly, the material properties, as well as temperature field are extrapolated in time. Then, a predicted velocity is computed solving $\boldsymbol{v}^*$ as

$$\rho^\dagger\left(\frac{a\boldsymbol{v}^*+b\boldsymbol{v}^n+c\boldsymbol{v}^{n-1}}{\Delta t}+\boldsymbol{\nabla}\cdot\left(\boldsymbol{v}^\dagger\otimes\boldsymbol{v}^*\right)-\boldsymbol{v}^*\boldsymbol{\nabla}\cdot\boldsymbol{v}^\dagger\right)=-\boldsymbol{\nabla}p^n+\boldsymbol{\nabla}\cdot\left(\mu^\dagger\dot{\boldsymbol{\gamma}}^*\right)-\frac{2}{3}\boldsymbol{\nabla}\left(\mu^\dagger\boldsymbol{\nabla}\cdot\boldsymbol{v}^*\right)+\rho^\dagger\boldsymbol{g}\,, \tag{16}$$

with the generic non-homogeneous Dirichlet boundary condition $\boldsymbol{v^*} \cdot \boldsymbol{n} = \boldsymbol{v}_0 \cdot \boldsymbol{n}$ at the boundary of the domain, denoted by Γ.

Then, the resolution of the pressure increment field is made by solving

$$\frac{a\varphi}{(\rho c^2)^\dagger \Delta t} - \boldsymbol{\nabla} \cdot \left(k_\varphi^\dagger \boldsymbol{\nabla} \varphi\right) = -\boldsymbol{\nabla} \cdot \boldsymbol{v}^* + \dot{S}_\varphi^\dagger \,, \tag{17}$$

with the homogeneous Neumann boundary condition $\frac{\partial \varphi}{\partial n} = 0$ at the boundary Γ (since $\boldsymbol{v^{n+1}} \cdot \boldsymbol{n} = \boldsymbol{v^*} \cdot \boldsymbol{n}$ and given (10)).

After solving φ, velocity and pressure are updated during a correction step as,

$$\boldsymbol{v}^{n+1} = \boldsymbol{v}^* - k_\varphi^\dagger \boldsymbol{\nabla} \varphi \,, \tag{18}$$

$$p^{n+1} = p^n + \varphi \,. \tag{19}$$

Once the velocity and pressure are corrected, the next step is to compute the corresponding temperature field using the (c_p, T) formulation of the energy conservation. The following is written in an implicit form

$$\begin{aligned} &\rho^\dagger c_p^\dagger \left(\frac{aT^{n+1} + bT^n + cT^{n-1}}{\Delta t} + \left(\boldsymbol{\nabla} \cdot (\boldsymbol{v} T) - T \boldsymbol{\nabla} \cdot \boldsymbol{v}\right)^{n+1} \right) \\ &\quad - T^{n+1} \beta_p^\dagger \left(\frac{ap^{n+1} + bp^n + cp^{n-1}}{\Delta t} + \boldsymbol{v}^{n+1} \cdot \boldsymbol{\nabla} p^{n+1} \right) = \boldsymbol{\nabla} \cdot (\lambda^\dagger \boldsymbol{\nabla} T^{n+1}) + \Phi_d^{n+1} \,. \end{aligned} \tag{20}$$

Finally, our pressure-based method uses the EoS to update the density and thermophysical properties of the fluid just before moving to the next time iteration:

$$x^{n+1} = \mathrm{EoS}(T^{n+1}, p^{n+1}) \,. \tag{21}$$

3.3. Note on the treatment of the volume penalization method

The immersed boundary of a solid can be treated by adding a volume penalization term $\chi\,(\boldsymbol{v} - \boldsymbol{v_0})$ to the right hand side of the momentum equation. On a Cartesian grid and obstacles whose boundaries are parallel to the grid directions, a large value (10^{20}) of the parameter χ allows to assign the velocity $\boldsymbol{v}$ equal to the given velocity $\boldsymbol{v_0}$.

In such an approach, the incremental pressure correction method needs to be slightly corrected in order to maintain a Neumann boundary condition on the pressure increment at the immersed boundary. It can be easily shown that $k_\varphi^\dagger$ coefficient has to be replaced by

$$k_\varphi^\dagger = \frac{\Delta t}{a\rho^\dagger + \chi \Delta t} \,. \tag{22}$$

In a finite volume code, a large value of χ on the face of the cell at the boundary (geometrically interpolated from cell centre values) penalized the pressure increment derivative to zero and thus unconnect fluid and solid domains. This method converges spatially at first-order only. This method can be easily implemented by considering a Jacobi linear system preconditioning that locally reduces matrix coefficient to 1 instead of a value around 10^{20}.

4. Numerical methods

The novel method presented above has been implemented in an in-house CFD code developed in Fortran 2008 under a free software license, named `Notus` [46]. `Notus` employs the Finite Volume Method on a Cartesian staggered grid, allowing simulation of multiphysical problems such as single-phase and multiphase flows with both mass and heat transfer.

In pursuit of computational efficiency and scalability, the code is designed for high-performance parallel computing up to petascale simulations [47]. The pressure-velocity coupling for multiphase flows is achieved through the incremental pressure correction methods originally developed by Goda [27]. For monophasic flows, the rotational incremental pressure correction method of Timmermans et al. [28] is employed, ensuring better convergence orders.

Notus offers both first-order (Euler backward) and second-order temporal discretization with Backward Differentiation Formula (BDF2). For the governing equations, implicit discretization (centered second-order, upwind first and second-order) as well as explicit schemes, including Weighted Essentially Non-Oscillatory (WENO) and Lax-Wendroff (LW) with Total Variation Diminishing (TVD) schemes, are available. This flexibility caters to a diverse range of CFD applications. For all the presented test cases in this article, an implicit second-order scheme is used for the advection terms, diffusion, and stress terms. BDF2 second-order time discretization is also employed, except when specifically mentioned for the first-order Euler scheme. The advected pressure gradient term of (15) is discretized with upwind second-order scheme and a decentering at boundaries of the domain to avoid boundary condition on pressure.

Notus utilizes advanced iterative solvers and multigrid preconditioners within the Hypre library [48], or it can use direct solvers from the MUMPS library [49]. The credibility and reliability of the code are established through a thorough verification, validation, and non-regression environment. Notus has been widely used in various scientific contexts [47, 50, 51, 52, 53, 54].

5. Verification

Verification and validation of a CFD code are essential steps in establishing a reliable numerical tool. These concepts are extensively discussed in [55] and [56], and are more broadly addressed in [57]. Verification is the process of determining whether the implementation of a model and its associated methods accurately represents its conceptual description and solution. The fundamental strategy of verification involves the identification, quantification, and reduction of errors in the numerical model and its solution. Code verification encompasses solution verification on a set of problems for which the exact solution (available only for simplified problems) is known or manufactured. The latter does not necessarily require a connection with the reality of a physical phenomenon. Verification thus offers evidence that the continuous model is correctly solved by the discrete approach chosen in the calculation code. It is primarily a mathematical and computational process.

For each verification test case of this section, we present convergence studies considering an analytical solution. Tables of the section present absolute euclidean norm $||\varepsilon_X||_{\mathrm{L}_2}$, infinity norm $||\varepsilon_X||_{\mathrm{L}_\infty}$ of the field X and the respective orders of convergence.

5.1. Isentropic injection in a square cavity

As a first verification test case, we present the isentropic injection problem. A square cavity of length $L=1$ mm is filled with air considered as a perfect gas ($R=287\ \mathrm{J\,K^{-1}\,kg^{-1}}$, $\gamma=c_p/c_v=1.4$). At initial time, the following thermodynamic state is imposed $(T_0,p_0,\rho_0)=(300\mathrm{K}, 101325\mathrm{Pa}, \frac{p_0}{RT_0})$. A fluid in the same thermodynamic state as the cavity is injected from the top with a vertical velocity $\boldsymbol{v}_{y_0} = -1.0\times10^{-2}\ \mathrm{m\,s^{-1}}$. The dimensionless parameters of the problem are respectively the initial Reynolds, Mach and Prandtl numbers $\mathrm{Re}_0 = \rho_0 u_0 L/\mu_0 = 6.36\times10^{-1}$, $\mathrm{Ma}_0 = u_0/c_0 = 5.37\times10^{-4}$, $\mathrm{Pr}_0=c_p\mu_0/\lambda_0=7.04\times10^{-1}$.

The analytical solution of the problem can be found from [58]. Under the Stokes hypothesis ($\mathrm{Re}\le 1$), the test case exhibits a linear velocity field $\boldsymbol{v}_y=-v_0 y/L$, with a constant velocity divergence $\boldsymbol{\nabla}\cdot\boldsymbol{v}=-v_0/L$. Considering our hypothesis, equation (1a) reduce to $\frac{1}{\rho}\frac{\mathrm{d}\rho}{\mathrm{d}t}=v_0$ and after integration we obtain $\rho/\rho_0=\exp(v_0(t-t_0)/L)$. Using the law of reversible adiabatic process, *i.e.* $p\rho^{-\gamma}=\mathrm{cst}$, and the perfet gas EoS, the thermodynamic solution of the problem starting at $t_0=0\,\mathrm{s}$ reads to

$$p = p_0\exp(\gamma t v_0/L)\,, \tag{23a}$$
$$T = T_0\exp((\gamma-1)t v_0/L)\,, \tag{23b}$$
$$\rho = \rho_0\exp(t v_0/L)\,. \tag{23c}$$

Thermodynamic variables do not vary in space (0D benchmark) allowing temporal convergence study without any effect of spatial error (linear velocity).

For velocity boundary conditions, left and right boundaries have slip conditions, top has a Dirichlet condition for injection $\boldsymbol{v}_{top}=[0,-v_0]^T$ and bottom has a no-slip condition. For temperature boundary conditions, all the boundaries have homogeneous Neumann conditions.

Table 1 presents the temporal convergence study. Temporal second-order is achieved for pressure, density and temperature, for both L_2 and L_∞ norms. We do not present velocity errors in the table

Δt in s	$\|\|\varepsilon_p\|\|_{\mathrm{L}_2}$	order	$\|\|\varepsilon_p\|\|_{\mathrm{L}_\infty}$	order	$\|\|\varepsilon_T\|\|_{\mathrm{L}_2}$	order
4.00×10^{-4}	1.352×10^{-2}	n/a	1.352×10^{1}	n/a	3.278×10^{-7}	n/a
2.00×10^{-4}	3.389×10^{-3}	1.996	3.389	1.996	8.157×10^{-8}	2.007
1.00×10^{-4}	8.482×10^{-4}	1.998	8.483×10^{-1}	1.998	2.037×10^{-8}	2.001
5.00×10^{-5}	2.120×10^{-4}	2.000	2.121×10^{-1}	2.000	5.144×10^{-9}	1.986
2.50×10^{-5}	5.284×10^{-5}	2.004	5.294×10^{-2}	2.002	1.339×10^{-9}	1.942
1.25×10^{-5}	1.304×10^{-5}	2.019	1.314×10^{-2}	2.010	3.859×10^{-10}	1.794

Δt in s	$\|\|\varepsilon_T\|\|_{\mathrm{L}_\infty}$	order	$\|\|\varepsilon_\rho\|\|_{\mathrm{L}_2}$	order	$\|\|\varepsilon_\rho\|\|_{\mathrm{L}_\infty}$	order
4.00×10^{-4}	3.278×10^{-4}	n/a	1.076×10^{-7}	n/a	1.076×10^{-4}	n/a
2.00×10^{-4}	8.157×10^{-5}	2.007	2.696×10^{-8}	1.996	2.696×10^{-5}	1.996
1.00×10^{-4}	2.038×10^{-5}	2.001	6.749×10^{-9}	1.998	6.750×10^{-6}	1.998
5.00×10^{-5}	5.150×10^{-6}	1.984	1.687×10^{-9}	2.000	1.688×10^{-6}	1.999
2.50×10^{-5}	1.345×10^{-6}	1.937	4.209×10^{-10}	2.003	4.218×10^{-7}	2.001
1.25×10^{-5}	3.924×10^{-7}	1.777	1.043×10^{-10}	2.013	1.051×10^{-7}	2.004

Table 1: Temporal order accuracy of the isentropic injection test case. First time step $\Delta t = 4\times10^{-4}$ s equal to CFL $= 1.78\times10^{4}$. Mesh size 128^2, $t_f = 1\times10^{-1}$ s.

because, whatever the time step, the exact velocity is reached as expected with errors close to the resolution tolerance of linear systems (10^{-14}). As the problem is 1D for velocity and 0D for the other variables, conclusions do not change whatever be the mesh size form 8^2 to 128^2. Let us note the significant variations in pressure, temperature and density, final values at time $t_f = 1\times10^{-1}$ being 3.0955×10^5 Pa, 4.4755×10^2 K and 3.1988 kg m^{-3}, respectively.

5.2. Linear acoustic pulse propagation

The second test case investigates the isothermal problem of a linear acoustic wave propagation considering an inviscid perfect gas fluid ($\mu = 0$) with its EoS

$$\Delta p = c_0^2 \Delta \rho \,, \tag{24}$$

with Δp the pressure perturbation, $\Delta \rho$ the density perturbation and $c_0 = \sqrt{\gamma R T_0}$ the constant speed of sound of the medium. This benchmark has been used in the past to test several novel compressible solvers [14, 35, 26, 33, 19], often to carry out temporal convergence studies. Besides its simplicity and the existence of analytical solutions, this case allows a clear evaluation of the numerical diffusion and dispersion of the proposed numerical schemes.

We consider a monodimensional periodic domain of length $L = 1$ m. For velocity boundary conditions, left and right boundaries have periodic conditions while top and bottom have slip conditions. At initial time, we consider the thermodynamic state $(T_0, p_0, \rho_0) = (300\mathrm{K}, 10^5\mathrm{Pa}, \frac{p_0}{RT_0})$ and a Gaussian acoustic pressure wave defined as

$$p(x, t_0) = p_0 + \Delta p_0 \exp(-\frac{x^2}{2\Sigma^2}) \,, \tag{25}$$

with Δp_0 the pulse amplitude and Σ a pulse length control parameter. The initial parameter of the pulse is set to $\Delta p_0 = 10^2$ Pa and $\Sigma = 0.1$ m like in [33]. The dimensionless parameters of the problem are respectively $\mathrm{Re}_0 = \infty$ and $\mathrm{Ma}_0 = 7.14\times10^{-4}$.

From the resolution of the d'Alembert equation, analytical solutions are available for all fields. The pressure, density and velocity solutions are respectively

$$p(x, t) = p_0 + \Delta p_0 \exp\left(-\frac{(x - c_0 t)^2}{2\Sigma^2}\right) \,, \tag{26}$$

$$\rho(x, t) = \rho_0 + \frac{\Delta p_0}{c_0^2} \exp\left(-\frac{(x - c_0 t)^2}{2\Sigma^2}\right) \,, \tag{27}$$

$$u(x, t) = \frac{\Delta p_0}{\rho_0 c_0^2} \exp\left(-\frac{(x - c_0 t)^2}{2\Sigma^2}\right) \,. \tag{28}$$

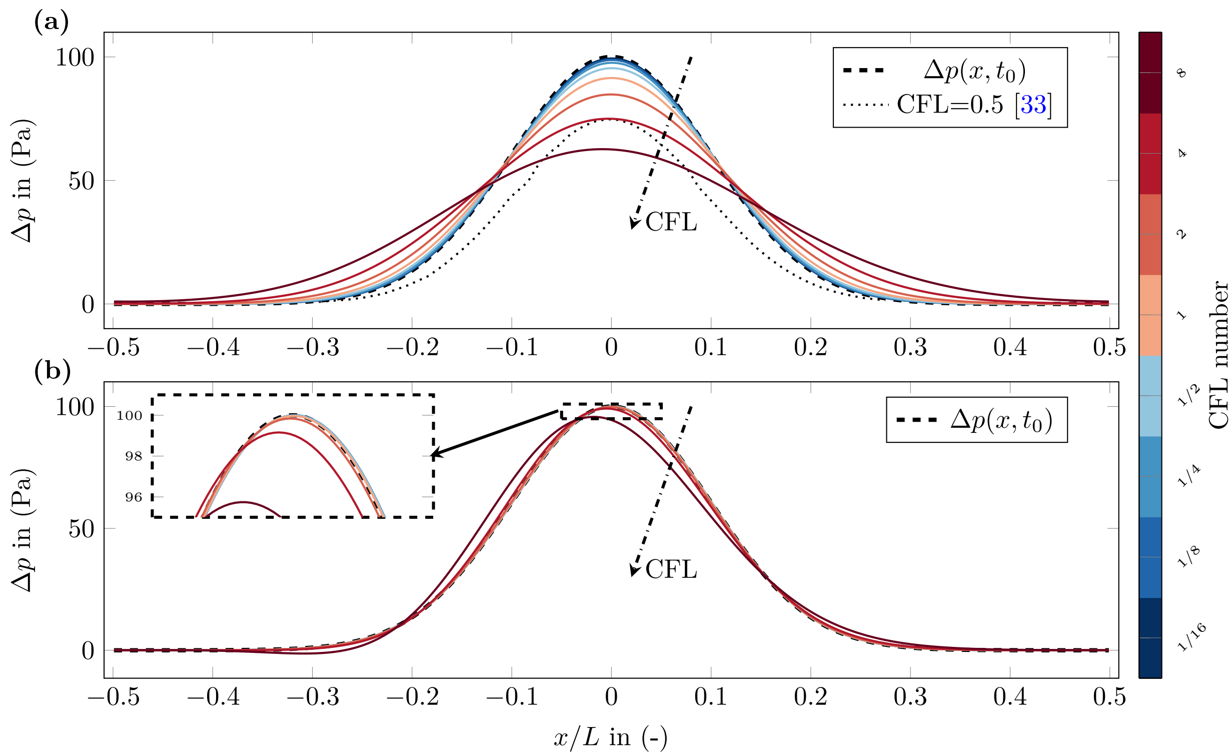

Figure 1: Acoustic pressure field variation at initial state $t = 0$ s (dashed line) and at $t_f = 2.88 \times 10^{-3}$ s for various $\mathrm{CFL} = \Delta t c_0/\Delta x$ (solid line colored by CFL value). (a) Euler backward temporal scheme. (b) BDF2 temporal scheme. Mesh size 512x8.

with $c_0 t$ the distance travelled by the wave.

Figure 1a presents a graphical temporal convergence study of the relative pressure field at $t_f = c_0/L = 2.88 \times 10^{-3}$ s (time travelled by the wave until it returns to its initial position) for various acoustic Courant number, noted CFL. The implicit treatment of pressure increment avoids a stability limitation related to acoustic time step as we do not find any stability limit (still stable at CFL $\sim 4 \times 10^3$ data not shown). For very large CFL and Euler backward temporal scheme, the acoustic wave is totally diffused but, note that for $\mathrm{CFL} = 4, 8$ the wave is still well predicted. We observe the relative low diffusivity of the first-order temporal scheme Euler backward at $\mathrm{CFL} = 4$ compared to literature results [33] which obtain similar value of the maximum of the relative pressure with a low Courant number value (see $\mathrm{CFL} = 0.5$ numerized curve from [33] in Fig. 1a).

Additionally, in Fig. 1b, it is noteworthy that the BDF2 scheme, with second-order temporal accuracy, exhibits significantly lower numerical diffusion compared to the Euler scheme. This results in a pressure profile that closely aligns with the exact solution at $\mathrm{CFL} = 2$. An error of less than 1% is observed compared to 20% with the Euler scheme. Using the BDF2 temporal scheme, the correct observation of acoustic propagation is possible while considering CFLs greater than unity.

In Table 2, the temporal convergence study of this test case with the BDF2 scheme is presented with a final time $t_f = L/c_s = 2.88 \times 10^{-3}$ s. Second-order temporal convergence is confirmed for pressure, velocity, and density, for both L_2 and L_∞ norms. We also present in Tab. 3 the spatial convergence study with a constant Courant number $\mathrm{CFL} = 1$. Second-order spatial convergence is confirmed for all fields considering both L_2 and L_∞ norms.

5.3. Manufactured solutions

The technique known as the method of manufactured solutions involves the development of an *a priori* known analytical solutions for the governing equations. The procedure introduces modifications of the original equations (1) by adding source term on the right-hand side of equations (see Appendix B). These source terms are considered as input, for reproducing the manufactured solution.

Δt in s	$\|\|\varepsilon_v\|\|_{\mathrm{L}_2}$	order	$\|\|\varepsilon_v\|\|_{\mathrm{L}_\infty}$	order	$\|\|\varepsilon_p\|\|_{\mathrm{L}_2}$	order
1.60×10^{-4}	4.568×10^{-2}	n/a	9.698×10^{-2}	n/a	1.842×10^{1}	n/a
8.00×10^{-5}	2.304×10^{-2}	0.987	5.057×10^{-2}	0.939	9.293	0.987
4.00×10^{-5}	7.871×10^{-3}	1.550	1.846×10^{-2}	1.454	3.176	1.549
2.00×10^{-5}	1.986×10^{-3}	1.987	4.873×10^{-3}	1.922	8.017×10^{-1}	1.986
1.00×10^{-5}	3.272×10^{-4}	2.601	7.510×10^{-4}	2.698	1.321×10^{-1}	2.601

Δt in s	$\|\|\varepsilon_p\|\|_{\mathrm{L}_\infty}$	order	$\|\|\varepsilon_\rho\|\|_{\mathrm{L}_2}$	order	$\|\|\varepsilon_\rho\|\|_{\mathrm{L}_\infty}$	order
1.60×10^{-4}	3.911×10^{1}	n/a	1.528×10^{-4}	n/a	3.245×10^{-4}	n/a
8.00×10^{-5}	2.039×10^{1}	0.940	7.710×10^{-5}	0.987	1.692×10^{-4}	0.940
4.00×10^{-5}	7.451	1.452	2.635×10^{-5}	1.549	6.182×10^{-5}	1.452
2.00×10^{-5}	1.968	1.920	6.651×10^{-6}	1.986	1.633×10^{-5}	1.920
1.00×10^{-5}	3.036×10^{-1}	2.697	1.096×10^{-6}	2.601	2.519×10^{-6}	2.697

Table 2: Temporal order accuracy of the linear acoustic pulse test case. First time step $\Delta t = 1.6\times10^{-4}$ s equal to CFL$=2.84\times10^{1}$. Mesh size 512×8, $t_f=2.88\times10^{-3}$ s.

Mesh	$\|\|\varepsilon_v\|\|_{\mathrm{L}_2}$	order	$\|\|\varepsilon_v\|\|_{\mathrm{L}_\infty}$	order	$\|\|\varepsilon_p\|\|_{\mathrm{L}_2}$	order
16x8	5.723×10^{-2}	n/a	1.115×10^{-1}	n/a	2.308×10^{1}	n/a
32x8	3.040×10^{-2}	0.913	6.849×10^{-2}	0.704	1.226×10^{1}	0.913
64x8	1.089×10^{-2}	1.481	2.650×10^{-2}	1.370	4.394	1.488
128x8	2.852×10^{-3}	1.933	6.872×10^{-3}	1.947	1.151	1.933
256x8	5.231×10^{-4}	2.446	1.181×10^{-3}	2.540	2.113×10^{-1}	2.444
512x8	1.382×10^{-4}	1.921	2.832×10^{-4}	2.061	5.567×10^{-2}	1.922

Mesh	$\|\|\varepsilon_p\|\|_{\mathrm{L}_\infty}$	order	$\|\|\varepsilon_\rho\|\|_{\mathrm{L}_2}$	order	$\|\|\varepsilon_\rho\|\|_{\mathrm{L}_\infty}$	order
16x8	4.378×10^{1}	n/a	1.915×10^{-4}	n/a	3.632×10^{-4}	n/a
32x8	2.804×10^{1}	0.643	1.017×10^{-4}	0.913	2.326×10^{-4}	0.643
64x8	1.067×10^{1}	1.394	3.645×10^{-5}	1.481	8.853×10^{-5}	1.394
128x8	2.768	1.947	9.550×10^{-6}	1.932	2.296×10^{-5}	1.947
256x8	4.768×10^{-1}	2.537	1.753×10^{-6}	2.446	3.955×10^{-6}	2.537
512x8	1.140×10^{-1}	2.064	4.619×10^{-7}	1.924	9.457×10^{-7}	2.064

Table 3: Spatial order accuracy of the linear acoustic pulse test case. Courant number CFL$=1$, $t_f=2.88\times10^{-3}$ s.

In literature, few manufactured solutions for compressible subsonic flows have been developed [59, 36, 37, 18] to validate novel algorithms. After a detailed analysis of the nature and properties of already proposed solutions, we aim to define a generic, well posed, and reproducible manufactured solution (see Appendix B). We thus propose the following two-dimensional compressible Navier–Stokes solution for a perfect gas in a square domain $\Omega = [0,1] \times [0,1]$ where the pressure $p(x,y,t)$, the temperature $T(x,y,t)$, the density $\rho(x,y,t)$ and the velocity $\boldsymbol{u}=(u,v)^T$ read to

$$p = p_0 + p_1 \sin(\pi y) \sin(\pi x) \cos(2\pi f t)\,, \tag{29a}$$

$$T = T_0 + T_1 \sin(\pi y) \cos(\pi x) \cos(2\pi f t)\,, \tag{29b}$$

$$\rho = p/RT\,, \tag{29c}$$

$$u = u_0 \sin^2(\pi x) \sin(2\pi y) \cos(2\pi f t)\,, \tag{29d}$$

$$v = u_0 \sin(2\pi x) \sin^2(\pi y) \cos(2\pi f t)\,, \tag{29e}$$

with f the frequency in Hz, p_0 and p_1 the reference and fluctuation pressure in Pa, T_0 and T_1 the reference and fluctuation temperature K, u_0 the reference velocity in $\mathrm{m\,s^{-1}}$ and R the universal gas constant in $\mathrm{J\,K^{-1}\,kg^{-1}}$. The perfect gas EoS permits the verification of the solver with time- and space-dependent material properties, except for dynamic viscosity and conductivity considered as constant here.

The proposed solution is derived from the manufactured solution initially proposed for incompressible flows [29]. One notices good properties of the solution to simulate a subsonic flow with incremental pressure correction method as the non-zero pressure gradient at boundary or the non-zero divergence field. Time-dependent Dirichlet boundary conditions are applied for temperature fields. For velocity boundary conditions, all the boundaries have no-slip conditions while Neumann homogeneous boundary condition is imposed on pressure increment.

To investigate the accuracy of the resolved fields and different ranges of dimensionless parameters, three specific manufactured solutions are introduced in the following three subsections by tuning parameters. It is helpful to test the proposed method on low Mach solution as encountered in compressible natural flows (*e.g.* $\mathrm{Ma}_0 \simeq 1\times10^{-3}$), as well on solution with much larger Mach (*e.g.* $\mathrm{Ma}_0 \simeq 0.6$), The following parameters will remain constant for all three cases : $f = 700$ Hz, $p_0 = 10^5$ Pa, $p_1 = 2\times10^3$ Pa, $T_0 = 300$K, $R = 287\ \mathrm{J\,K^{-1}\,kg^{-1}}$, $\gamma = 1.4$. $\mu = 1.85\times10^{-5}$ Pa s. All the convergence studies consider the final time $t_f = 2\times10^{-3}$ s corresponding more than one and a half times the period $T = 1/f$.

5.3.1. Isothermal high Mach subsonic manufactured solution

The isothermal flow case considers the following parameters $T_1 = 0$ K, $u_0 = 200\ \mathrm{m\,s^{-1}}$. We present this unsteady flow solution for whoever wants to analyse the temporal order without considering the coupling of the Navier–Stokes equations and the energy equation. The dimensionless parameters of this case are $\mathrm{Re}_0 = 1.26\times10^7$, $\mathrm{Ma}_0 = 5.76\times10^{-1}$.

Table 4 presents the temporal convergence study. Second-order convergence in time is achieved for velocity, pressure, and density, considering both the L_2 and L_∞ norms.

5.3.2. Anisothermal high Mach subsonic manufactured solution

A fully compressible subsonic case is now studied considering the following parameters $T_1 = 40$ K, $u_0 = 200\ \mathrm{m\,s^{-1}}$, $\lambda = 10^{-2}\mathrm{W\,m^{-1}\,K^{-1}}$. We investigate temporal order of convergence on a test case with the following dimensionless parameters: $\mathrm{Re}_0 = 1.26\times10^7$, $\mathrm{Ma}_0 = 5.76\times10^{-1}$ and $\mathrm{Pr}_0 = 1.86$.

Firstly, we present in Fig 2 the variations of the primitive variables of the proposed anisothermal manufactured solution. Fig 2a,b,c,d show respectively pressure, temperature, divergence and velocity fields while Fig 2e,f present respectively the local variations of Mach and Reynolds numbers. One may notice strong divergence variations (see Fig 2c) and a maximal local Mach number at $t = 0$ s of 0.6 (see Fig 2e), twice the incompressible limit.

We present in Table 5 the temporal convergence study of the case. The proposed method reaches the temporal second-order for all the resolved fields, for both L_2 and L_∞ norms. We also present in Tab. 6 the spatial convergence study with a constant Courant number of CFL = 1 for each simulation necessary to attenuate the temporal error. Second-order spatial convergence is also confirmed for all fields considering both L_2 and L_∞ norms.

Δt in s	$\|\|\varepsilon_v\|\|_{\mathrm{L}_2}$	order	$\|\|\varepsilon_v\|\|_{\mathrm{L}_\infty}$	order	$\|\|\varepsilon_p\|\|_{\mathrm{L}_2}$	order
2.00×10^{-4}	3.932×10^{1}	n/a	6.442×10^{1}	n/a	5.853×10^{3}	n/a
1.00×10^{-4}	1.497×10^{1}	1.393	2.570×10^{1}	1.326	1.861×10^{3}	1.653
5.00×10^{-5}	4.289	1.803	7.931	1.696	5.325×10^{2}	1.805
2.50×10^{-5}	1.120	1.938	2.116	1.906	1.402×10^{2}	1.925
1.25×10^{-5}	2.882×10^{-1}	1.958	5.489×10^{-1}	1.947	3.594×10^{1}	1.964
6.25×10^{-6}	7.739×10^{-2}	1.897	1.479×10^{-1}	1.892	9.641	1.898

Δt in s	$\|\|\varepsilon_p\|\|_{\mathrm{L}_\infty}$	order	$\|\|\varepsilon_\rho\|\|_{\mathrm{L}_2}$	order	$\|\|\varepsilon_\rho\|\|_{\mathrm{L}_\infty}$	order
2.00×10^{-4}	1.467×10^{4}	n/a	6.798×10^{-2}	n/a	1.704×10^{-1}	n/a
1.00×10^{-4}	4.935×10^{3}	1.572	2.161×10^{-2}	1.653	5.731×10^{-2}	1.572
5.00×10^{-5}	1.625×10^{3}	1.602	6.185×10^{-3}	1.805	1.887×10^{-2}	1.602
2.50×10^{-5}	4.387×10^{2}	1.889	1.629×10^{-3}	1.925	5.095×10^{-3}	1.889
1.25×10^{-5}	1.131×10^{2}	1.956	4.175×10^{-4}	1.964	1.313×10^{-3}	1.956
6.25×10^{-6}	3.006×10^{1}	1.911	1.120×10^{-4}	1.898	3.492×10^{-4}	1.911

Table 4: Temporal order accuracy of the isothermal manufactured solution. First time step $\Delta t = 2\times10^{-4}$ s equal to CFL$=1.78\times10^{1}$. Mesh size 256^2 and $t_f = 2\times10^{-3}$ s.

Δt in s	$\|\|\varepsilon_v\|\|_{\mathrm{L}_2}$	order	$\|\|\varepsilon_v\|\|_{\mathrm{L}_\infty}$	order	$\|\|\varepsilon_p\|\|_{\mathrm{L}_2}$	order	$\|\|\varepsilon_p\|\|_{\mathrm{L}_\infty}$	order
2.00×10^{-4}	3.753×10^{1}	n/a	7.456×10^{1}	n/a	6.230×10^{3}	n/a	1.975×10^{4}	n/a
1.00×10^{-4}	1.366×10^{1}	1.458	2.493×10^{1}	1.581	1.885×10^{3}	1.724	5.279×10^{3}	1.904
5.00×10^{-5}	3.874	1.818	6.913	1.850	5.200×10^{2}	1.858	1.548×10^{3}	1.770
2.50×10^{-5}	1.012	1.936	1.843	1.907	1.352×10^{2}	1.944	4.018×10^{2}	1.946
1.25×10^{-5}	2.600×10^{-1}	1.961	4.832×10^{-1}	1.932	3.438×10^{1}	1.975	1.059×10^{2}	1.924
6.25×10^{-6}	6.917×10^{-2}	1.910	1.324×10^{-1}	1.868	9.065	1.923	2.881×10^{1}	1.878

Δt in s	$\|\|\varepsilon_T\|\|_{\mathrm{L}_2}$	order	$\|\|\varepsilon_T\|\|_{\mathrm{L}_\infty}$	order	$\|\|\varepsilon_\rho\|\|_{\mathrm{L}_2}$	order	$\|\|\varepsilon_\rho\|\|_{\mathrm{L}_\infty}$	order
2.00×10^{-4}	7.616	n/a	3.153×10^{1}	n/a	5.457×10^{-2}	n/a	1.978×10^{-1}	n/a
1.00×10^{-4}	2.519	1.596	8.642	1.867	1.711×10^{-2}	1.673	4.451×10^{-2}	2.152
5.00×10^{-5}	6.835×10^{-1}	1.882	2.403	1.847	4.728×10^{-3}	1.856	1.385×10^{-2}	1.684
2.50×10^{-5}	1.767×10^{-1}	1.952	6.304×10^{-1}	1.930	1.234×10^{-3}	1.938	4.020×10^{-3}	1.785
1.25×10^{-5}	4.528×10^{-2}	1.964	1.617×10^{-1}	1.963	3.159×10^{-4}	1.966	1.084×10^{-3}	1.890
6.25×10^{-6}	1.222×10^{-2}	1.889	4.300×10^{-2}	1.911	8.418×10^{-5}	1.908	3.079×10^{-4}	1.816

Table 5: Temporal order accuracy of the anisothermal high Mach subsonic manufactured solution. First time step $\Delta t = 2\times10^{-4}$ s equal to CFL$=1.78\times10^{1}$. Mesh size 256^2 and $t_f = 2\times10^{-3}$ s.

Mesh	$\|\|\varepsilon_v\|\|_{\mathrm{L}_2}$	order	$\|\|\varepsilon_v\|\|_{\mathrm{L}_\infty}$	order	$\|\|\varepsilon_p\|\|_{\mathrm{L}_2}$	order	$\|\|\varepsilon_p\|\|_{\mathrm{L}_\infty}$	order
64x64	3.055	n/a	5.712	n/a	3.811×10^{2}	n/a	1.125×10^{3}	n/a
128x128	8.000×10^{-1}	1.933	1.517	1.913	9.913×10^{1}	1.943	3.041×10^{2}	1.888
256x256	2.022×10^{-1}	1.984	3.911×10^{-1}	1.956	2.494×10^{1}	1.991	7.787×10^{1}	1.965
512x512	5.094×10^{-2}	1.989	9.963×10^{-2}	1.973	6.254	1.995	2.035×10^{1}	1.936

Mesh	$\|\|\varepsilon_T\|\|_{\mathrm{L}_2}$	order	$\|\|\varepsilon_T\|\|_{\mathrm{L}_\infty}$	order	$\|\|\varepsilon_\rho\|\|_{\mathrm{L}_2}$	order	$\|\|\varepsilon_\rho\|\|_{\mathrm{L}_\infty}$	order
64x64	5.259×10^{-1}	n/a	1.835	n/a	3.572×10^{-3}	n/a	1.088×10^{-2}	n/a
128x128	1.348×10^{-1}	1.963	4.789×10^{-1}	1.938	9.270×10^{-4}	1.946	3.054×10^{-3}	1.833
256x256	3.394×10^{-2}	1.990	1.216×10^{-1}	1.978	2.338×10^{-4}	1.987	8.115×10^{-4}	1.912
512x512	8.539×10^{-3}	1.991	3.841×10^{-2}	1.662	5.892×10^{-5}	1.988	2.805×10^{-4}	1.533

Table 6: Spatial order accuracy of the anisothermal high Mach subsonic manufactured solution. Courant number CFL$=1$ and $t_f = 2\times10^{-3}$ s.

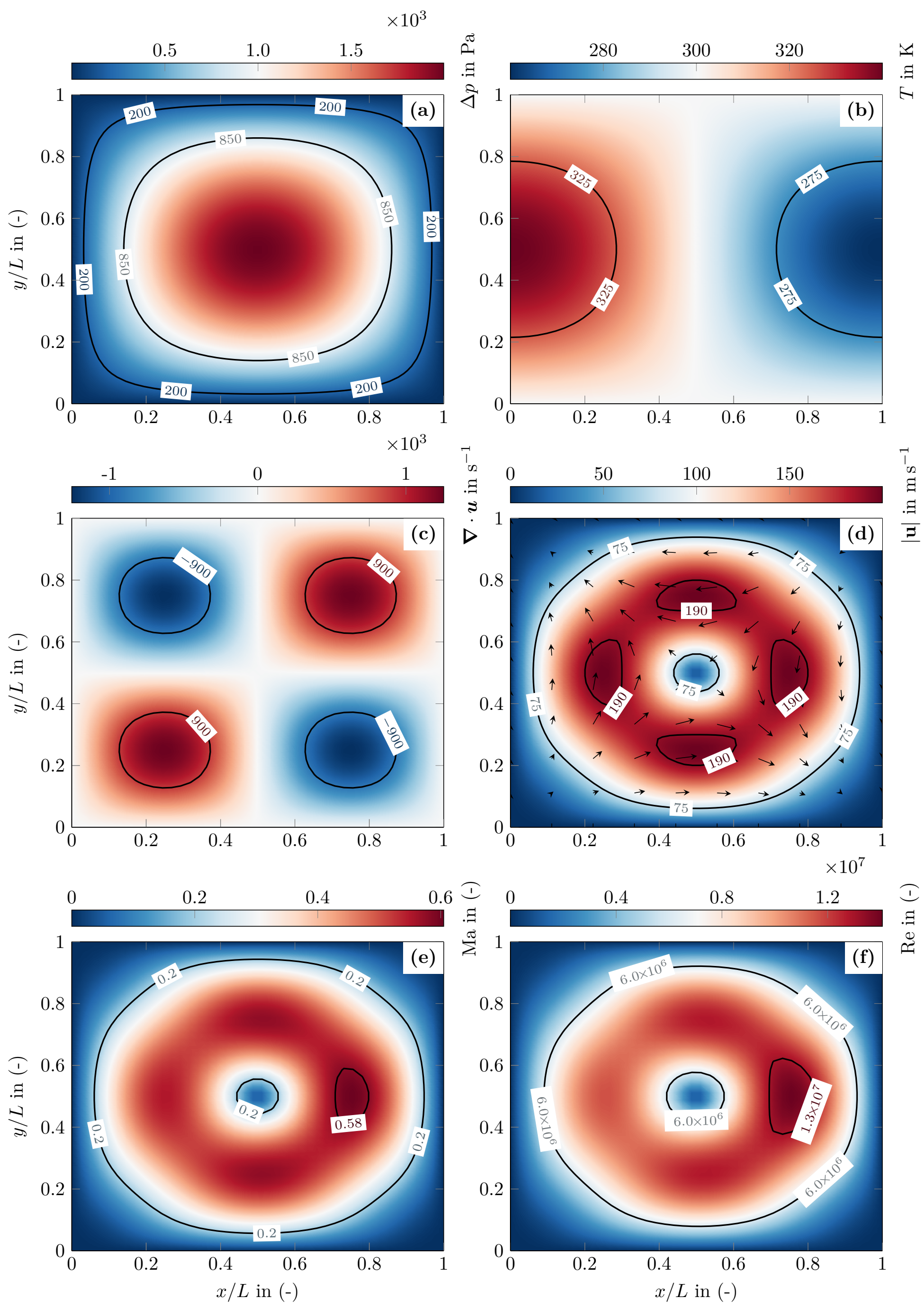

Figure 2: Visualisation of the high Mach anisothermal solution within the square domain $\Omega = [0,1] \times [0,1]$ at $t = 0$ s. (a) Relative pressure field $\Delta p = p - p_0$. (b) Temperature field T. (c) Divergence of the velocity field $\boldsymbol{\nabla} \cdot \boldsymbol{u}$. (d) Velocity vector field $\boldsymbol{u}$ (arrows) and its magnitude $||\boldsymbol{u}||$. (e) Local Mach number Ma. (f) Local Reynolds number Re.

Δt in s	$\|\|\varepsilon_v\|\|_{\mathrm{L}_2}$	order	$\|\|\varepsilon_v\|\|_{\mathrm{L}_\infty}$	order	$\|\|\varepsilon_p\|\|_{\mathrm{L}_2}$	order	$\|\|\varepsilon_p\|\|_{\mathrm{L}_\infty}$	order
2.00×10^{-4}	3.732×10^{-1}	n/a	8.834×10^{-1}	n/a	2.155×10^{2}	n/a	4.502×10^{2}	n/a
1.00×10^{-4}	1.392×10^{-1}	1.423	3.185×10^{-1}	1.472	6.529×10^{1}	1.723	1.552×10^{2}	1.537
5.00×10^{-5}	4.116×10^{-2}	1.758	9.162×10^{-2}	1.798	1.830×10^{1}	1.835	5.266×10^{1}	1.559
2.50×10^{-5}	1.105×10^{-2}	1.897	2.398×10^{-2}	1.934	4.728	1.952	1.438×10^{1}	1.873
1.25×10^{-5}	2.894×10^{-3}	1.933	6.335×10^{-3}	1.921	1.196	1.983	3.774	1.930
6.25×10^{-6}	8.596×10^{-4}	1.751	1.840×10^{-3}	1.784	3.346×10^{-1}	1.838	1.179	1.678

Δt in s	$\|\|\varepsilon_T\|\|_{\mathrm{L}_2}$	order	$\|\|\varepsilon_T\|\|_{\mathrm{L}_\infty}$	order	$\|\|\varepsilon_\rho\|\|_{\mathrm{L}_2}$	order	$\|\|\varepsilon_\rho\|\|_{\mathrm{L}_\infty}$	order
2.00×10^{-4}	4.166	n/a	1.349×10^{1}	n/a	1.857×10^{-2}	n/a	6.571×10^{-2}	n/a
1.00×10^{-4}	8.746×10^{-1}	2.252	2.500	2.432	3.712×10^{-3}	2.323	1.190×10^{-2}	2.465
5.00×10^{-5}	1.903×10^{-1}	2.201	4.338×10^{-1}	2.527	7.819×10^{-4}	2.247	2.099×10^{-3}	2.503
2.50×10^{-5}	4.569×10^{-2}	2.058	1.232×10^{-1}	1.816	1.816×10^{-4}	2.106	5.321×10^{-4}	1.980
1.25×10^{-5}	1.139×10^{-2}	2.004	3.835×10^{-2}	1.683	4.416×10^{-5}	2.040	1.577×10^{-4}	1.754
6.25×10^{-6}	2.871×10^{-3}	1.988	1.485×10^{-2}	1.369	1.089×10^{-5}	2.020	5.649×10^{-5}	1.481

Table 7: Temporal order accuracy of the anisothermal low Mach manufactured solution. First time step $\Delta t = 2\times10^{-4}$ s equal to $\mathrm{CFL} = 1.78\times10^{1}$. Mesh size 256^2 and $t_f = 2\times10^{-3}$ s.

5.3.3. Anisothermal low Mach subsonic manufactured solution

A low Mach fully compressible subsonic case in now studied considering the following parameters $T_1 = 40$ K, $u_0 = 2$ m s^{-1}, $\lambda = 10^{-2}$ W m^{-1} K^{-1}. We investigate temporal order of convergence on a test case with the following dimensionless parameters: $\mathrm{Re}_0 = 1.26\times10^{5}$, $\mathrm{Ma}_0 = 5.76\times10^{-3}$ and $\mathrm{Pr}_0 = 1.86$,

We present in Table 7 the temporal convergence study of the case. The method reaches the temporal second-order for all the resolved fields, for both L_2 and L_∞ norms.

6. Validation

Validation is the process that assesses the extent to which a numerical model accurately represents a physical phenomenon for the purpose of utilizing the results. It entails comparing precise numerical solutions with experimental (or theoretical) results. It's important to note that validation doesn't assume the experimental measurements are inherently more accurate than the numerical solutions; rather, it considers them as the most adequate means available for representing the reality in the context of validation. Benchmarking the numerical solutions obtained with different codes is also a crucial component of the validation process.

The validation section is structured around both stationary and unsteady test cases. Initially, the proposed method is validated on a well-known low Mach compressible steady natural convection benchmark, encompassing cases with constant and variable viscosity. Following that, validation is extended to a natural convection test case in the presence of an immersed boundary. In the second part, validation is conducted on two unsteady 1D thermoacoustic wave generation and propagation scenarios. The first involves a Dirichlet boundary condition and a perfect gas, while the second incorporates a heat flux and operates very close to the liquid-vapor critical point. Finally, validation is carried out on a 2D unsteady natural convection case at a Mach number of 0.1.

6.1. Compressible steady natural convection benchmark

Compressible flows can occur due to large temperature variations, resulting in large density changes for which the Boussinesq approximation and thus the incompressible assumption is no longer valid. In this section, we validate the proposed method by reproducing the classical *case T1* and *case T2* steady-state benchmarks of Le Quéré et al. [15]. From the nomenclature of [15], *case T1* refers to constant viscosity and conductivity while the *case T2* considers Sutherland law for viscosity and conductivity (see Appendix C for parameters values). We thus consider a differentially heated square cavity of length L subject to gravitational field $\boldsymbol{g}$, filled with air considered as a perfect gas, with the following initial dimensionless parameters: temperature ratio $\epsilon = \frac{T_{\mathrm{hot}} - T_{\mathrm{cold}}}{T_{\mathrm{hot}} + T_{\mathrm{cold}}} = 0.6$, Rayleigh number $\mathrm{Ra}_0 = \mathrm{Pr}_0 \frac{g \Delta T L^3 \beta_{p_0} \rho_0^2}{\mu_0^2} = 10^6$, Prandtl number $\mathrm{Pr}_0 = 7.1\times10^{-1}$. Initial Mach number (considering the characteristic velocity $u_0 = \frac{\lambda_0}{\rho_0 c_p L}\sqrt{\mathrm{Ra}_0}$ [60]) are $\mathrm{Ma}_0 = 1.78\times10^{-3}$ for *case T1* and $\mathrm{Ma}_0 = 2.15\times10^{-3}$ for *case T2*, respectively.

Mesh	Nusselt (left)	order	Nusselt (right)	order	Mean relative pessure in Pa	order
64x64	9.0509	n/a	9.0811	n/a	-1.7907×10^{4}	n/a
128x128	8.9110	n/a	8.9184	n/a	-1.5438×10^{4}	n/a
256x256	8.8711	1.810	8.8728	1.834	-1.4809×10^{4}	1.971
512x512	8.8598	1.821	8.8602	1.864	-1.4669×10^{4}	2.170
1024x1024	8.8564	1.741	8.8565	1.770	-1.4643×10^{4}	2.452
Extrapolation	8.8550	n/a	8.8550	n/a	-1.4637×10^{4}	n/a

Mesh	Mean velocity in $\mathrm{m\,s^{-1}}$	order	Mean temperature in K	order
64x64	4.9700×10^{-2}	n/a	5.6453×10^{2}	n/a
128x128	4.8601×10^{-2}	n/a	5.6823×10^{2}	n/a
256x256	4.8313×10^{-2}	1.929	5.6930×10^{2}	1.791
512x512	4.8245×10^{-2}	2.077	5.6957×10^{2}	1.967
1024x1024	4.8230×10^{-2}	2.183	5.6964×10^{2}	1.995
Extrapolation	4.8225×10^{-2}	n/a	5.6966×10^{2}	n/a

Table 8: Spatial order accuracy of the compressible natural convection *case T1* [15]. CFL$=$400, $t_f=20$ s .

The boundary conditions of both cases are as follows. For temperature, the top and bottom walls are adiabatic conditions and left and right have respectively heated and cooled $T_{\text{hot}} = 960$ K and $T_{\text{cold}} = 240$ K. For velocity boundary conditions, all the boundaries have no-slip conditions. Both cases have been simulated considering an adaptative time step driven by an acoustic CFL$=4\times10^2$. The implicit treatment of the pressure computation permits to consider large CFL number which amounts to naturally filtering acoustic waves.

The objective of the present validation is to compare the reference values of the spatial average side walls Nusselt numbers $\overline{\text{Nu}}_{\text{left,right}}$ and cavity maximal pressure at steady state from [15] with our simulations. We propose a final time $t_f=20$ s regarding the previous final time proposed [33] which verifies the steady state residuals of our simulations.

Figure 3a,b presents respectively the pseudocolor plot of temperature field along with the velocity vectors field of the *case T1* and the temperature profile comparison at $y=L/2$ between T1 and T2 cases. Simulation results of the T2 case [61, 62] are also plotted in Fig. 3b. The simulation of *case T2* with our full compressible modelling well reproduces the temperature profile solution [61, 62] while most of the benchmark contributions were obtained considering the low Mach number approximation [15, 62]. To the author's knowledge, temperature profile solution of the *case T1* is unavailable in the literature. We plot in Fig. 3b this horizontal temperature profile and we validate this case in the following regarding Nusselt number and maximal pressure. As this configuration is simpler than T2, this approach is acceptable.

We propose in Table 8 a spatial convergence study of *case T1* for regular meshes at CFL $= 400$ also with Richardson extrapolated values. We observe a spatial second-order convergence on Nusselt numbers, spatial averaged pressure, temperature, and velocity.

Reference values of T1 are $\bar{\text{Nu}}=8.859\,78$ and $p_{\max}/p_0=0.856\,338$ [15]. By carefully read the list of pitfalls and recommendations proposed by the authors of the benchmark [15], we verified the equality of the averaged left and right Nusselt number which for 1024^2 mesh are identical to three significant digits ($\overline{\text{Nu}}_L - \overline{\text{Nu}}_R = 9.48\times10^{-5}$).

On the mesh size 1024^2, we found for the maximal pressure $p_{\max}/p_0 = 0.855\,486$. According to reference values [15], the absolute relative differences are respectively 9.95×10^{-2} % for the maximal pressure and 3.76×10^{-2} % for the Nusselt number (left value chosen).

Table 9 shows the spatial convergence study of *case T2* for regular meshes at CFL$=$400 also with Richardson extrapolated values. Here, spatial second-order is observed on spatial averaged relative pressure, temperature and velocity, and varying between 1.63-1.85 for left and right Nusselt numbers. Reference values of this case are $\overline{\text{Nu}} = 8.6866$ and $p_{\max}/p_0 = 0.924\,487$ [15]. On the mesh size 1024^2, we found for the maximal pressure $p_{\max}/p_0 = 0.923\,744$ and for the absolute difference between left and right Nusselt number 1.4×10^{-4}. According to reference values [15], the relative differences are respectively 7.4×10^{-4} % for the maximal pressure and 7.8×10^{-4} % for the Nusselt number (left value chosen).

In addition to the classical presented data for this benchmark, we propose in Fig. 4a the local Mach number at steady state of the *case T1* computed as $\text{Ma} = \sqrt{u^2+v^2}/\sqrt{\gamma RT}$. We observe the

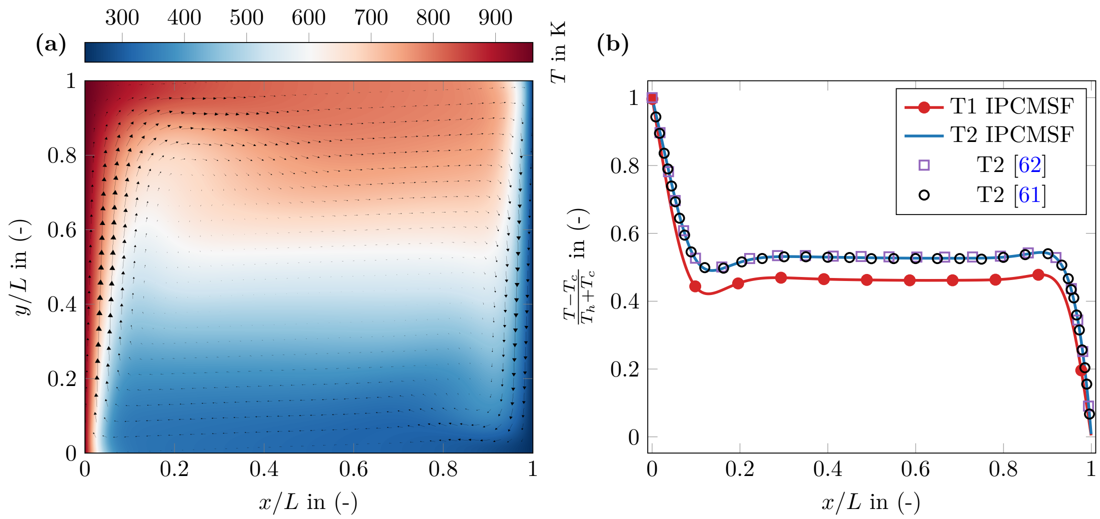

Figure 3: (a) Pseudocolor plot of temperature field and velocity vectors field of the *case T1* [15]. (b) Horizontal dimensionless temperature profile $T(x, y = L/2)/T_0$ comparison between T1 (circle symbols) and T2 (solid line) cases. Vierendeels et al. [61] *case T2* simulation (circle symbols), Kuan and Szmelter [62] *case T2* simulation (rectangle symbols). Simulation results of *case T2* [61, 62] are also plotted in Fig. 3b. CFL = 400, mesh size 1024^2, $t_f = 20$ s.

Mesh	Nusselt (left)	order	Nusselt (right)	order	Mean relative pessure in Pa	order
64x64	9.0067	n/a	9.0350	n/a	-1.1448×10^{4}	n/a
128x128	8.7767	n/a	8.7881	n/a	-8.9730×10^{3}	n/a
256x256	8.7129	1.852	8.7155	1.765	-8.0069×10^{3}	1.357
512x512	8.6924	1.634	8.6930	1.689	-7.7715×10^{3}	2.037
1024x1024	8.6858	1.644	8.6860	1.682	-7.7269×10^{3}	2.401
Extrapolation	8.6827	n/a	8.6828	n/a	-7.7164×10^{3}	n/a

Mesh	Mean velocity in m s^{-1}	order	Mean temperature in K	order
64x64	5.6898×10^{-2}	n/a	5.9958×10^{2}	n/a
128x128	5.6037×10^{-2}	n/a	6.0538×10^{2}	n/a
256x256	5.5683×10^{-2}	1.285	6.0746×10^{2}	1.478
512x512	5.5585×10^{-2}	1.848	6.0808×10^{2}	1.740
1024x1024	5.5562×10^{-2}	2.059	6.0825×10^{2}	1.847
Extrapolation	5.5554×10^{-2}	n/a	6.0832×10^{2}	n/a

Table 9: Spatial order accuracy of the compressible natural convection case T2 [15]. CFL = 400, $t_f = 20$ s.

maximal Mach number values in the both sidewall boundary layers of $\mathrm{Ma}_{\max} = 4.5\times10^{-4}$. We do not find back the Ma_0 assumed by the characteristic velocity coming from the current dimensional analysis [60]. The current range of local Mach is one order of magnitude below the expected value, *i.e.* $\mathrm{Ma}_0 = 1.78\times10^{-3}$. The characteristic velocity overestimates the true characteristic velocity, whether it is calculated [63, 60, 64]. This remark is valid also for the others natural convection benchmarks proposed below (Section 6.3.3 and Section 6.2). In addition to the local Mach number, we report the maximum and minimum values of the velocity divergence at steady state, $(\boldsymbol{\nabla}\cdot\boldsymbol{v})_{\max} = 12.97\ \mathrm{s}^{-1}$ (left bottom of the cavity) and $(\boldsymbol{\nabla}\cdot\boldsymbol{v})_{\min} = -9.571\ \mathrm{s}^{-1}$ (top right of the cavity). Without giving additional plotting, extreme values give another measure of the compressibility of the flow in addition to local Mach number.

6.2. Immersed boundary compressible steady natural convection benchmark

Natural convection in a cavity induced by an immersed heating body is considered in this section. The steady test case from Bouafia and Daube [63] is considered with the following dimensionless parameters $\mathrm{Ra}_0 = 5\times10^6$, $\mathrm{Re}_0 = 2.65\times10^3$, $\mathrm{Ma}_0 = 1.53\times10^{-3}$, $\mathrm{Pr}_0 = 7.1\times10^{-1}$, $\varepsilon = 0.2$ with the reference velocity computed as $V_0 = \frac{\mu_0}{\rho_0 L}\sqrt{\mathrm{Ra}_0}$ [63]. We refer the reader to the original paper [63] for the geometrical configuration. The fluid filling the square cavity is air with variable Sutherland law for viscosity and conductivity (see Appendix C for parameters values). We propose for our simulations an acoustic CFL=400 and a final time $t_f = 30$ s which verifies the steady state residuals of our simulations. A spatial first-order volume-penalty method is used [65] (see Section 3.3).

For temperature, the top and bottom walls are adiabatic conditions, left and right boundaries are cooled and the immersed boundary is heated ($T_{\mathrm{hot}} = 360$ K and $T_{\mathrm{cold}} = 240$ K). For velocity boundary conditions, no slip conditions are considered.

Figure 5a,b presents respectively horizontal profiles of dimensionless velocity and temperature and the pseudocolor plot of temperature field and velocity vectors field at the steady state. The characteristic flow described by Bouafia and Daube [63], under a low Mach numerical method, is exactly found back by our simulations with the two counter-rotating recirculation zones cut off by a central plume induced by the heated immersed boundary (see Figure 5b). More importantly, the flow symmetry along the central vertical axis at this Rayleigh number is observed in Fig 5a,b and in Fig 4c. A discrepancy is visible for both velocity and temperature horizontal profiles (Figure 5a) between the literature data [63] and our simulation on the mesh 1024^2. We report our 1024^2 mesh as spatially converged and we note that Bouafia's data are very close to those produced by our 512^2 mesh (data not shown).

We present the local Mach number at steady state in Fig. 4b. The maximum Mach number ($\mathrm{Ma}_{\max} = 5.3\times10^{-4}$) are located in the area of the central vertical thermal plume. As remarked in Section 6.1, the range of local Mach is one order of magnitude below the expected value, *i.e.* $\mathrm{Ma}_0 = 1.53\times10^{-3}$. In addition to the local Mach number and to give another measure of the compressibility of the flow, we report the maximum and minimum values of the velocity divergence at steady state, $(\boldsymbol{\nabla}\cdot\boldsymbol{v})_{\max} = 17.23\ \mathrm{s}^{-1}$ and $(\boldsymbol{\nabla}\cdot\boldsymbol{v})_{\min} = -15.03\ \mathrm{s}^{-1}$, located at the two upper corners of the heated immersed boundary.

As expected due to the immersed boundary method used, first convergence order is observed (Table 10) on averaged Nusselt numbers, spatial averaged relative pressure, velocity, and temperature. Richardson extrapolated values are also provided in the table. To the author's knowledge, Nusselt numbers of this benchmark have never been reported, both on the side walls (Table 10), but also on the hot Immersed Boundary (IB), *i.e.* $\mathrm{Nu}^{\mathrm{IB}}_{\mathrm{top}} = 1.1681\times10^1$, $\mathrm{Nu}^{\mathrm{IB}}_{\mathrm{bottom}} = 3.0025\times10^1$, $\mathrm{Nu}^{\mathrm{IB}}_{\mathrm{left}} = 3.1641\times10^1$, $\mathrm{Nu}^{\mathrm{IB}}_{\mathrm{right}} = 3.1641\times10^1$ on the finest grid. For all Nusselt computations, we consider the length of the cavity as the characteristic length. The high Nusselt numbers of left, right, and bottom IB express the very thin thermal boundary layer observed compared to the top IB thermal boundary layer (see Fig 5b). Absolute difference between left and right Nusselt number for the entire cavity and for the immersed boundary are respectively 1.41×10^{-4} and 1.2×10^{-11}.

6.3. Unsteady test cases

6.3.1. Thermoacoustic wave propagation in a perfect gas

The generation and propagation of thermoacoustic wave is the subject of the present test case introduced by Huang and Bau [66] and later studied by Farouk et al. [67]. A nitrogen-filled one-dimensional cavity of length $L = 1$mm is at the initial state $(T_0, p_0, \rho_0) = (300\mathrm{K}, 101325\mathrm{Pa}, \frac{p_0}{RT_0})$, where

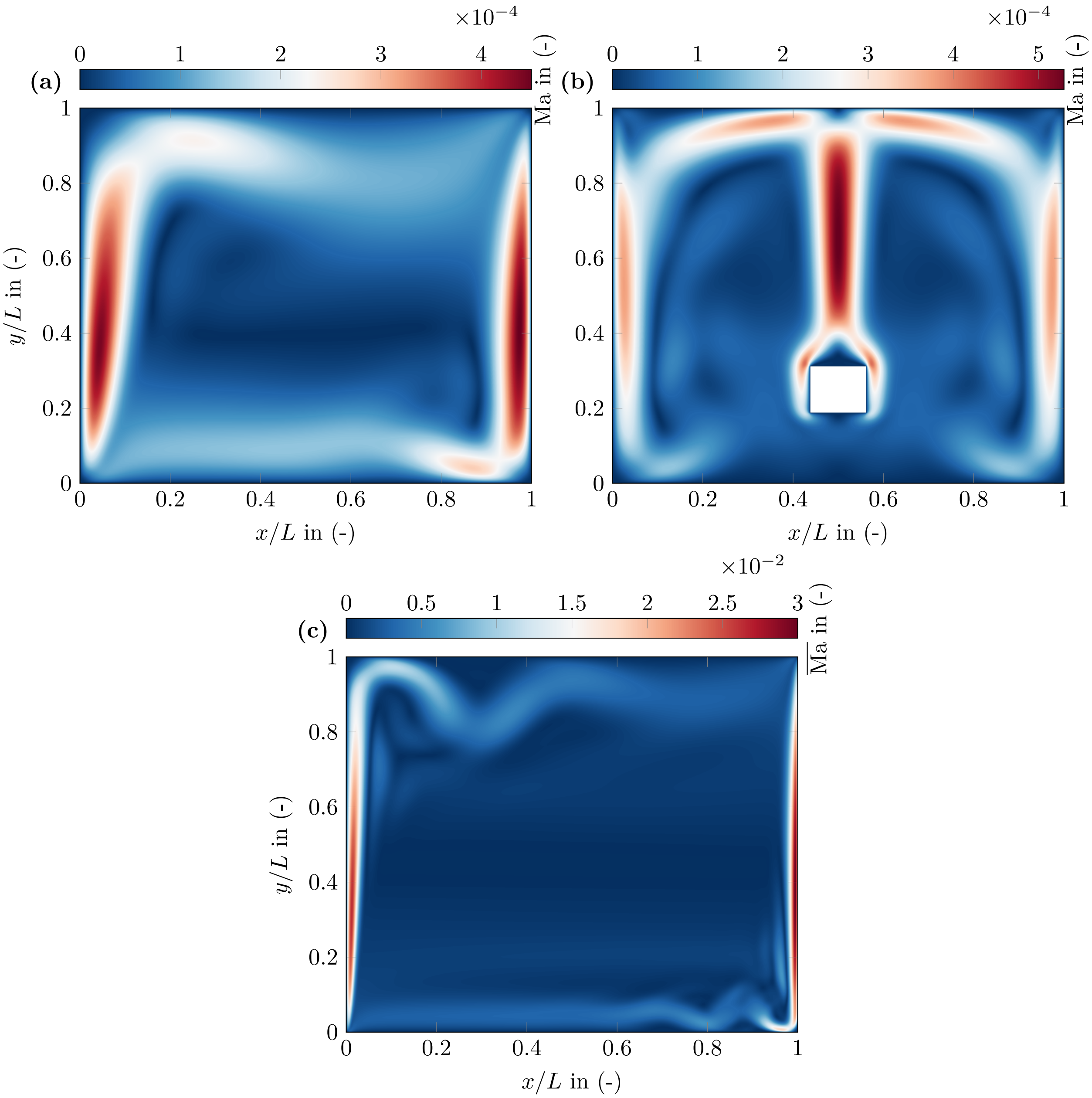

Figure 4: Local Mach number variations. (a) Steady compressible *case T1* benchmark [15]. Mesh size 1024^2, CFL$=$400, $t_f = 20$ s. (a) Steady immersed boundary compressible benchmark [63]. Mesh size 1024^2, CFL $= 400$, $t_f = 30$ s. (c) Time averaged Mach of the unsteady compressible benchmark [64]. CFL $= 2.5\times10^3$, Chebyshev mesh size 256^2, $t_f = 5.0051\times10^3$ s.

(a)

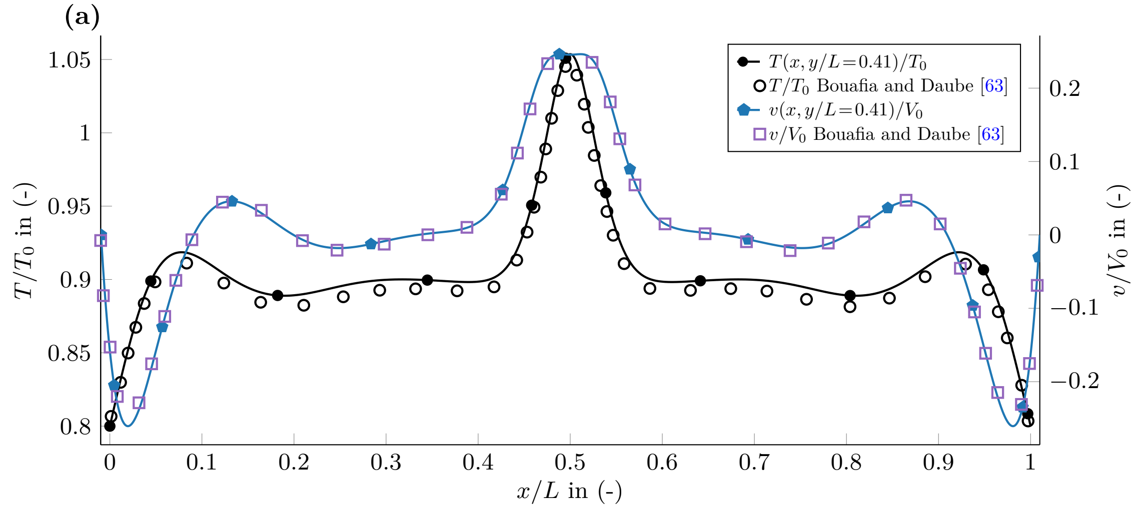

(b)

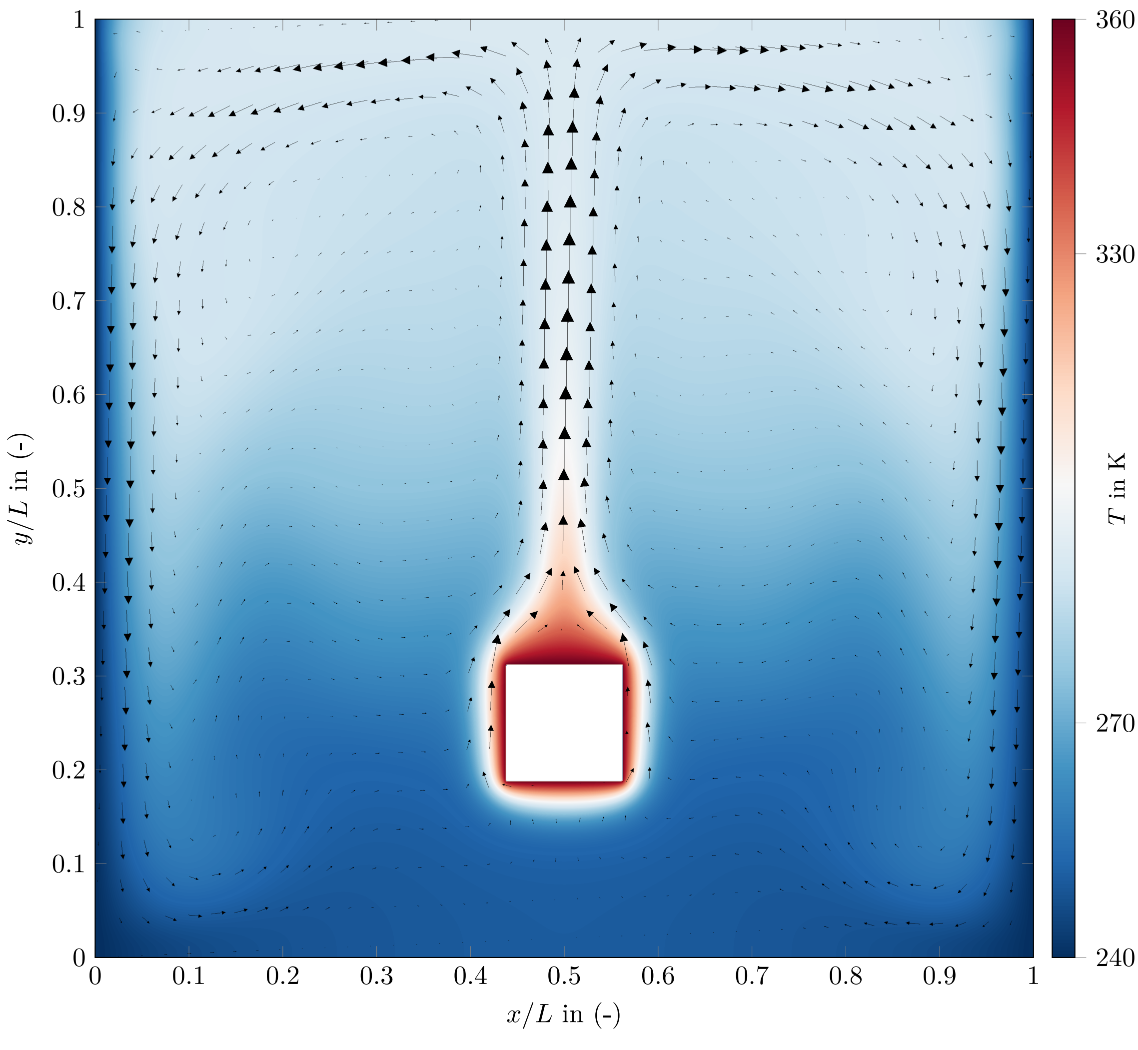

Figure 5: (a) Horizontal profiles of dimensionless temperature $T(x, y/L = 0.41)/T_0$ (left y-axis) and vertical velocity $v(x, y/L = 0.41)/V_0$ (right y-axis). (b) Pseudocolor plot of temperature field and velocity vectors field at stationarity. Mesh size 1024^2, CFL = 400, $t_f = 30$ s.

Mesh	Nusselt (left)	order	Nusselt (right)	order	Mean relative pressure in Pa	order
64x64	6.1467	n/a	6.1467	n/a	$-1.3617{\times}10^4$	n/a
128x128	6.4145	n/a	6.4145	n/a	$-1.0793{\times}10^4$	n/a
256x256	6.5442	1.046	6.5442	1.046	$-9.9263{\times}10^3$	1.705
512x512	6.6137	0.902	6.6137	0.902	$-9.5457{\times}10^3$	1.187
1024x1024	6.6502	0.926	6.6502	0.926	$-9.3550{\times}10^3$	0.997
Extrapolation	6.6908	n/a	6.6908	n/a	$-9.1636{\times}10^3$	n/a

Mesh	Mean velocity in $\mathrm{m\,s^{-1}}$	order	Mean temperature in K	order
64x64	$3.7091{\times}10^{-2}$	n/a	$2.6967{\times}10^2$	n/a
128x128	$3.7338{\times}10^{-2}$	n/a	$2.7219{\times}10^2$	n/a
256x256	$3.7498{\times}10^{-2}$	0.627	$2.7321{\times}10^2$	1.292
512x512	$3.7572{\times}10^{-2}$	1.122	$2.7366{\times}10^2$	1.197
1024x1024	$3.7606{\times}10^{-2}$	1.104	$2.7387{\times}10^2$	1.088
Extrapolation	$3.7636{\times}10^{-2}$	n/a	$2.7406{\times}10^2$	n/a

Table 10: Spatial order accuracy of the immersed boundary compressible natural convection [63]. CFL$=$400, $t_f=$30 s.

the gas is considered to be a perfect gas. The viscosity and conductivity of the fluid are temperature dependent (see Appendix C for parameters values). The validation of this test case is carried out by the comparison of our pressure wave profile at time $t = 0.25t_0 = 7.08{\times}10^{-7}$ s against reported data from simulations of the original paper [66] and from Farouk et al. [67]. The dimensionless parameters are respectively $\mathrm{Ma}_0 = 6.0{\times}10^{-2}$ (computed from velocity max peak at $t = 0.25t_0$ and the initial speed of sound $c_0 = \sqrt{\gamma R T_0}$) and $\mathrm{Pr}_0 = 0.75$.

For velocity boundary conditions, left and right boundaries have no-slip conditions while top and bottom boundaries have slip conditions. For temperature boundary conditions, top and bottom have homogeneous Neumann conditions, right and left have respectively Dirichlet condition with $T_R = T_0$ and $T_L(t > 0) = 2T_0$.

Figure 6 presents the thermoacoustic wave shape within the cavity at $t = 0.25t_0$ by plotting the dimensionless relative pressure along space for our simulation and literature data. This flow is characterized by the propagation of a pressure wave with a sharp front and an increasing peak width over time [66, 67]. Because of the strong heating on the left of the cavity and the ideal gas hypothesis, the wave speed is variable and its correct prediction is mandatory. An inconsistency between the two references about the wavefront and the speed of the wave can be seen in Fig. 6. The proposed solution (mesh size 32768×8 and CFL=0.1), resulting from a spatial and temporal comparative study, can be seen as a reference solution. It is possible to validate the propagation speed of the Huang and Bau [66] wave by comparison with our data. Note that for the two previous solutions [66, 67], the numerical diffusion explains the attenuated wave observed. The present benchmark permits to validate our method to simulate thermoacoustic wave propagation. In the next test case, we investigate the same phenomenon very close to the liquid-vapor critical point with a very low amplitude and sharp thermoacoustic wave propagation.

6.3.2. Thermoacoustic wave propagation close to the liquid-vapor critical point

Miura et al. [68] firstly study experimentally supercritical carbon dioxide acoustic wave propagation using a very sensitive interferometer to capture the piston effect within a cavity of length $L = 1.08$ cm. The reproduction of Miura et al. [68] experimental data has been the cornerstone for validation of a CFD code with applications in supercritical fluid dynamics [44, 69, 70]. On the critical isochore and very close to the critical point ($T_c = 304.13$ K, $\rho_c = 467.6\ \mathrm{kg\,m^{-3}}$, $p_c = 73.77$ bar), the authors reported the normalized variation of density $\frac{(\rho-\rho_0)}{\rho_0} \times 10^7$ along a period of time $t_f = 0.4$ ms when the left cavity is heated by a constant heat flux Φ_L during 0.2 ms. After this period, adiabatic condition is imposed to the left wall. The reproduction of Miura et al. [68] experimental data has been the cornerstone for validation of a CFD code with applications in supercritical fluid dynamics [44, 69, 70].

A simulation employing identical initial and boundary conditions as those observed in the experimental setup has been conducted within a one-dimensional domain. For the temperature boundary, we impose on the left wall a constant heat flux $\Phi_L = 1.83\ \mathrm{kW\,m^{-2}}$ during the first 0.2 ms and adiabatic condition to the right wall and left wall after $t > 0.2$ ms. For the velocity boundary, we impose slip

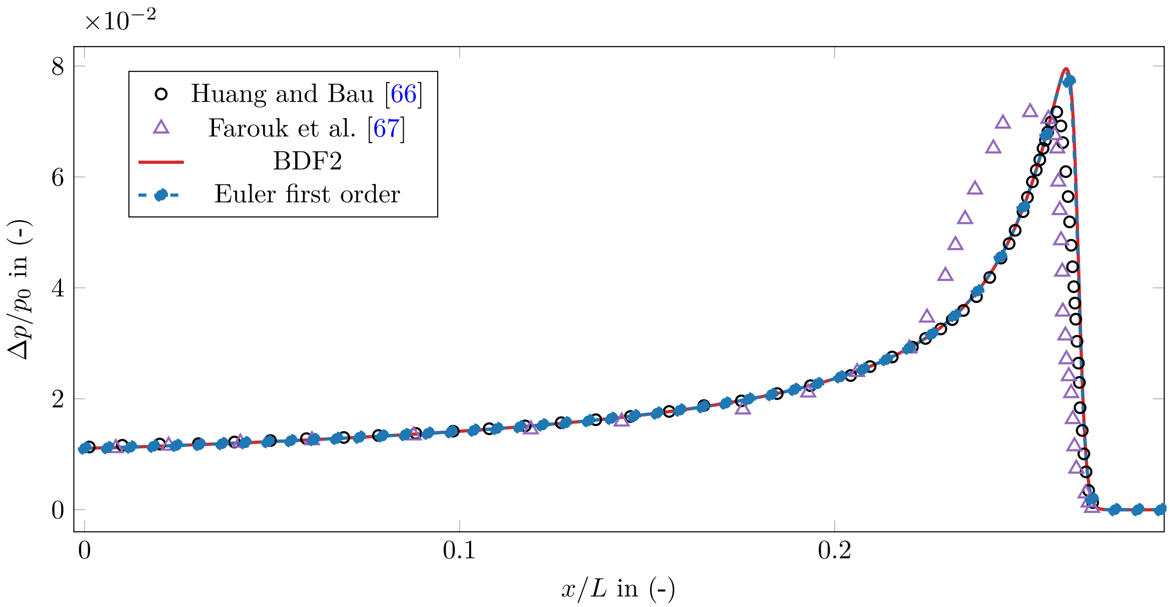

Figure 6: Comparison of dimensionless relative pressure wave at $t = 0.25t_0 = 7.08{\times}10^{-7}$ s. IPCMSF with BDF2 temporal scheme (solid line), IPCMSF with Euler backward temporal scheme (dashed line with symbol), simulation from Huang and Bau [66] (empty circle symbols), simulation from Farouk et al. [67] (empty triangle symbols). Mesh size 32768×8 and CFL=0.1.

condition to all boundaries. The NIST `refprop` library has been used as EoS to compute the density and all the thermophysical properties of the fluid.

According to the experiment and the simulations (see Fig. 7, 8), the wave propagates continuously between the left and right walls. This leads to an increase in bulk temperature and, consequently, an increase in density. The present test case is highly challenging given the very low variations in density (approximately $1{\times}10^{-7}$) and the sharp shape of the travelling wave.

Figure 7 presents the normalized density variation at the cell centre as a function of time of the $T_0 - T_c = 150$ m K experiment of Miura et al. [68]. The results with first-order Euler backward are found to be in excellent agreement with experimental results, as well as other numerical solutions, validating the proposed method for flows very close to the critical point. Let us note that we simulated this test case with BDF2 temporal scheme but because of the dispersivity of the scheme (see Fig. 1b) and the sharp shape of the wave, the travelling is reconstructed at CFL=1 with oscillations of the solution.

In addition of density variations and for the sake of reproducibility, Figure 8 shows the normalized variations of temperature and pressure at the centre of the cell. As we compute density solely from the NIST `refprop` database and given our excellent result on the density wave propagation, it means excellent pressure and temperature resolutions.

6.3.3. Compressible unsteady natural convection benchmark

The last challenging benchmark testing our method is a recently proposed unsteady differentially heated square cavity with large temperature variations problem [64]. A two-dimensional cavity is filled with a perfect gas fluid with variable viscosity and conductivity following Sutherland law (see Appendix C for parameters values). The dimensionless parameters of the reproduced benchmark are $\mathrm{Ra}_0 = 1.83{\times}10^8$, $\mathrm{Re}_0 = 1.61{\times}10^4$, $\mathrm{Ma}_0 = 1{\times}10^{-1}$ (considering the reference velocity $u_0 = \sqrt{2\varepsilon L g}$ [64]), $\mathrm{Pr}_0 = 7.1{\times}10^{-1}$, $\varepsilon = 0.6$. One can observe significantly larger Mach number compared to the Le Quéré et al. [15] benchmark (see Section 6.1), providing an interesting complementary validation test case for subsonic compressible methods.

Boundary conditions are nearly identical as in Section 6.1. We introduce time-dependent hot and

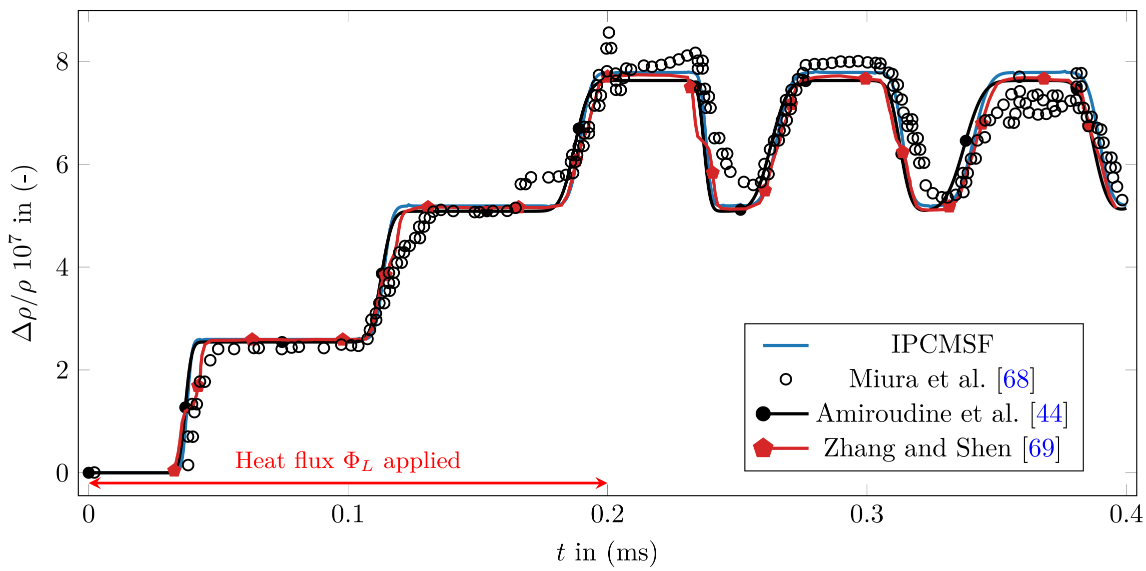

Figure 7: Comparison of normalized density variation between the experimental data at $\Delta T = 150$m K from the critical point and various numerical simulations. Numerized original experimental data [68] (empty circle symbols), IPCMSF with Euler backward temporal scheme (solid line) for a mesh size 1024×8 and CFL = 1, Amiroudine et al. [44] simulation (circle symbols), Zhang and Shen [69] simulation (pentagon symbols).

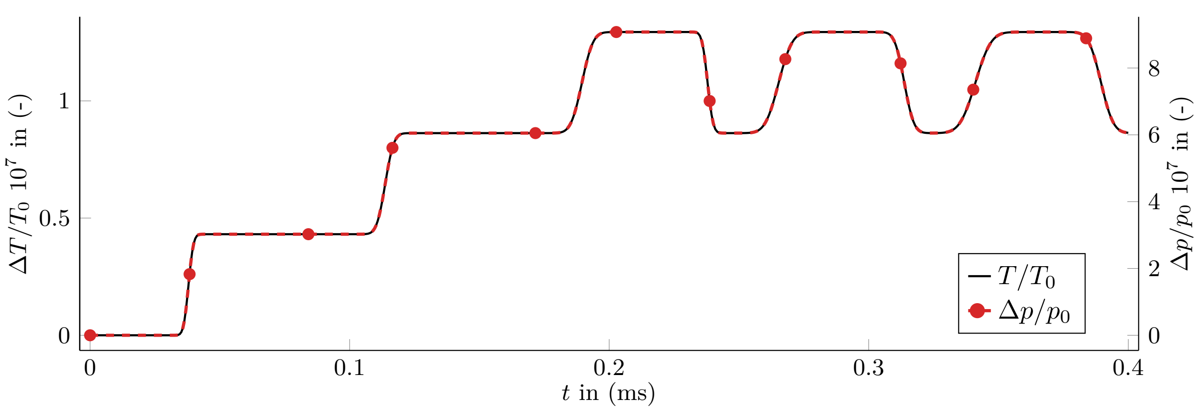

Figure 8: Thermodynamic variations at the cell center during the experiment of Miura et al. [68] at $\Delta T = 150$ m K from the critical point. Right y-axis: Normalized relative pressure (dashed line with symbols). Left y-axis: Normalized temperature (solid line).

cold temperature boundary conditions

$$T_L(t) = \frac{T_0 + T_L^\infty}{2} + \frac{T_0 - T_L^\infty}{2} \tanh(f_0(t - t_0)) \,, \tag{30}$$

$$T_R(t) = \frac{T_0 + T_R^\infty}{2} + \frac{T_0 - T_R^\infty}{2} \tanh(f_0(t - t_0)) \,, \tag{31}$$

with $f_0 = 2/t_0$ s^{-1} and $t_0 = 60$ s. $T_{L,R}(t)$ tend to $T_L^\infty = 960$ K and $T_R^\infty = 240$ K, respectively. The proposed time-dependent Dirichlet conditions $T_L(t)$ and $T_R(t)$ allow avoiding the stiff initialization during the first iterations of BDF2 simulations. The reported BDF2 stiffness of the constant left/right temperature boundary conditions leads to the divergence of the simulation appearing at the very first iterations. This diverging feature has not been observed with Euler backward temporal scheme due to the diffusion of the scheme. We do not report any difference that is induced by the temperature ramps on the periodically established flow solution.

Unlike the Le Quéré et al. [15] cases in Section 6.1, comparative results on regular and Chebychev mesh grids point out the necessity of Chebyshev grid refinement to well capture the very thin boundary layer of the test case (see Figure 9a,b). We present in the following results on a 256^2 Chebyshev refined mesh with an adaptative time step driven by an acoustic CFL=2.5×10^3.

For an ease of reproducibility, we report our statistic start time $t_s/t_{\text{eddy}} = 40$ and the end time $t_f/t_{\text{eddy}} = 100$ of the simulation, with $t_{\text{eddy}} = 4L/(3u_0)$ [64]. As performed by Wen et al. [64], we obtained a periodically established flow at this final time with relevant statistics of the resolved fields.

Figure 9a show the pseudocolor plot of the time averaged temperature and the velocity vector field at final time. In addition of the global overview of this natural convection benchmark and in order to provide reproducible data, we propose in Fig 9b three horizontal time averaged temperature profiles at final time along the vertical axis at $y=0.05L$, $y=0.5L$, $y=0.85L$, respectively.

Figure 9c,d show the time evolution of the instantaneous dimensionless velocity and temperature along the last five cycle. The localisation of the probes are for the temperature and velocity at $(x=0.85L, y=0.05L)$ and $(x=0.95L, y=0.05L)$, respectively. As found by Wen et al. [64], we find back two periodic signals of period $T = 1.85t_{\text{eddy}}$. Although we use a different numerical method, we observe an instantaneous temperature periodic temporal curve in good agreement with existing result [64]. Regarding the temporal evolution of instantaneous x-velocity (see Fig 9c), our temporal evolution during the period is relatively different from that reported although overall we find similar behavior. A possible reason is that we do not compare the temporal evolution of velocity at the same position in the cavity. In order to remove possible ambiguity on the location of the probes, we have marked them in Fig 9a.

We present the local time averaged Mach number at $t_f = 5.0051\times10^3$ s in Fig. 4c. The maximum Mach number ($\text{Ma}_{\max} = 3\times10^{-2}$) are located in the both very thin sidewall boundary layers as in Section 6.1. The range of local time averaged Mach is one order of magnitude below the expected value, *i.e.* Ma_0=0.1. Wen et al. [64] also document this discrepancy in the Mach order of magnitude on the Ra=5×10^9 case by plotting contour plot of local Mach number. In addition to the local Mach number, we report the maximum and minimum values of the instantaneous velocity divergence at final time, $(\boldsymbol{\nabla}\cdot\boldsymbol{v})_{\max} = 0.6146$ s^{-1} (left bottom of the cavity) and $(\boldsymbol{\nabla}\cdot\boldsymbol{v})_{\min} = -0.2980$ s^{-1} (right top of the cavity).

From data given by Wen et al. [64], the validation of this test case is achieved by the comparison of (a) the dimensionless temperature and velocity fluctuations spectrums, (b) the left and right time-averaged Nusselt number.

We present in Figure 9e,f the Power Density Spectrum (PDS) of the dimensionless velocity and temperature fluctuations fields. The reported PDS [64] of a field x is computed as $\text{PDS}_x = |\widehat{x}|^2$ with $\widehat{x}$ the Fast Fourier Transform (FFT) of x. We thus compute the dimensionless PDS of the time-varying x-velocity fluctuation as $\text{PDS}_u(f) = |\widehat{u'}|^2/u_0$, and temperature fluctuation $\text{PDS}_T(f) = |\widehat{T'}|^2/T_0$. For both x-velocity and temperature fluctuations, we found the first five dimensionless frequencies $\boldsymbol{f}\cdot t_{\text{eddy}} = (5.4\times10^{-1}, 1.0, 1.6, 2.2)^T$. Computed frequencies are consistent with reported values [64], *e.g.* the first frequency is in both studies $f_1 t_{\text{eddy}} \simeq 0.5$.

The left and right time-averaged Nusselts numbers computed on the last five cycles are respectively $\overline{\text{Nu}}_{\text{left}} = 34.73$, $\overline{\text{Nu}}_{\text{right}} = 34.66$. The absolute difference between left and right Nusselt is 7.44×10^{-2}. Our Nusselt numbers are consistent with the left reported value [64] of $\overline{\text{Nu}}_{\text{left}} = 34.2718$.

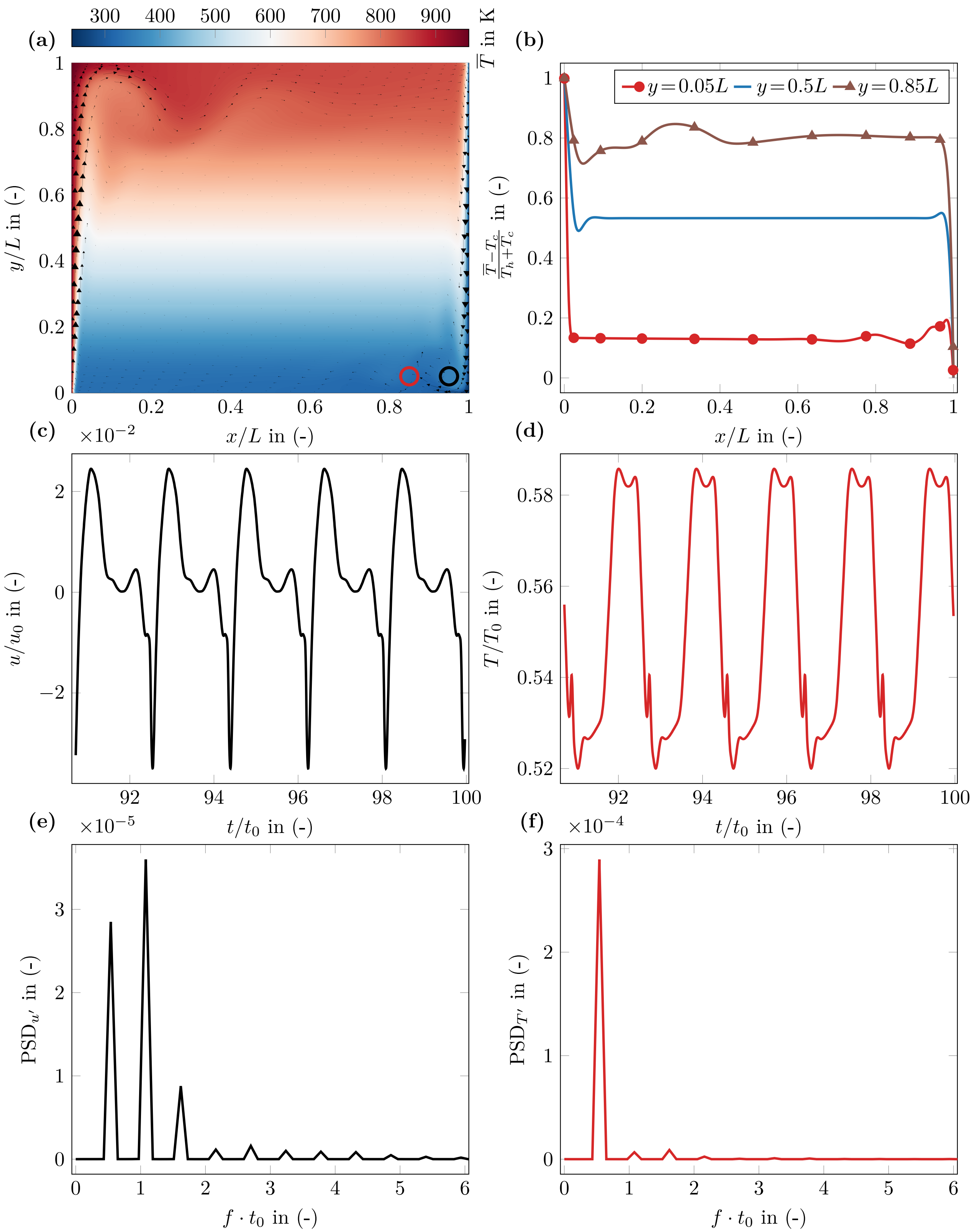

Figure 9: (a) Pseudocolor plot of time-averaged temperature field $\overline{T}(x, y)$ and velocity vectors field at $t_f = 5.0051\times10^3$ s. (b) Horizontal time-averaged dimensionless temperature profiles at differents vertical positions and at $t_f = 5.0051\times10^3$ s. (c) Time evolution of the instantaneous dimensionless x-velocity $u(x=0.95L, y=0.05L, t)/u_0$ during the last five periods. (d) Time evolution of the instantaneous dimensionless temperature $T(x = 0.85L, y = 0.05L, t)/T_0$ during the last five periods. (e) Power density spectrum of the dimensionless x-velocity flucturation FFT. (f) Power density spectrum of the dimensionless temperature flucturation FFT. CFL$=2.5\times10^3$, Chebyshev mesh size 256^2, $t_f = 100t_{\mathrm{eddy}} = 5.0051\times10^3$ s. The probes localisations for (c,e,d,f) plots are drawn on (a).

7. Conclusions and perspectives

In this article, we propose an original pressure-based method for compressible flows based on the temporal pressure increment. This can be sought as a generalization of the incremental pressure correction method of incompressible flows to compressible flows. The method has been spatially and temporally second-ordered verified, with solutions to flows with Mach number up to 0.6. The method is validated with both steady and unsteady compressible flows, featuring very large temperature ratio across the domain, thermoacoustic wave propagations in perfect gas as well as very close to the critical point where extremely low-density variations are encountered. The implicit resolution of pressure increment contributes to the increased numerical stability through the utilization of a very large CFL number whenever the nature of the test case allows for such a large time step, particularly in steady test cases. This results in significant computational time savings. Finally, when fluid properties satisfy the incompressible assumption, the method tends to the incompressible incremental pressure correction method.

The results obtained from the current work thus makes it feasible to advance this approach to more complex scenarios and physical problems such as flows with open and traction boundary conditions [71, 72], multiphase flows under the one-fluid compressible Navier-Stokes equations where both the phases could exhibit varying different compressibility and be governed by different equation of state, and reactive flows both in open and closed systems.

8. Acknowledgments

We acknowledge the French National Research Agency for its support (ANR-21-CE01-0018). This study received also financial support from the French government in the framework of the France 2030 program for University of Bordeaux / RRI BEST (french acronym for Research Network on Factory of the future). Numerical simulations were carried out using the facilities of the MCIA CURTA mesocentre.

Appendix A. Derivation of pressure-energy equation

This section presents the development of the energy conservation expressed in terms of pressure variable p. Starting from equation (7), whether we consider the conservation of energy in c_p formulation (1c) or in c_v formulation,

$$\rho c_v \left(\frac{\partial T}{\partial t} + \boldsymbol{v} \cdot \boldsymbol{\nabla} T \right) = -\frac{T\beta_p}{\chi_T} \boldsymbol{\nabla} \cdot \boldsymbol{v} + \boldsymbol{\nabla} \cdot (\lambda \boldsymbol{\nabla} T) + \Phi_d(\boldsymbol{v}) \,, \tag{A.1}$$

we obtain a unique equation of the conservation of energy expressed in pressure variable. In both cases, after introducing (A.1) or (1c) into equation (7) and grouping terms, we get

- in the c_v (A.1) formulation

$$\frac{\mathrm{d}p}{\mathrm{d}t} = -\left(\frac{1}{\chi_T} + \frac{T\beta_p^2}{\rho c_v \chi_T^2} \right) \boldsymbol{\nabla} \cdot \boldsymbol{v} + \frac{\beta_p}{\rho c_v \chi_T} \left(\boldsymbol{\nabla} \cdot (\lambda \boldsymbol{\nabla} T) + \Phi_d(\boldsymbol{v}) \right) \,, \tag{A.2}$$

- in the c_p (1c) formulation

$$\left(1 - \frac{T\beta_p^2}{\rho c_p \chi_T} \right) \frac{\mathrm{d}p}{\mathrm{d}t} = -\frac{1}{\chi_T} \boldsymbol{\nabla} \cdot \boldsymbol{v} + \frac{\beta_p}{\rho c_p \chi_T} \left(\boldsymbol{\nabla} \cdot (\lambda \boldsymbol{\nabla} T) + \Phi_d(\boldsymbol{v}) \right) \,. \tag{A.3}$$

It can be demonstrated that equations (A.2) and (A.3) are identical using several thermodynamic relations, *i.e.* Mayer relation $T\beta_p^2/(\rho c_v \chi_T) = \gamma - 1$, ratios of specific heats $\gamma = c_p/c_v$, definition of the speed of sound $c^2 = 1/(\chi_s \rho)$, permit to write

$$\frac{1}{\chi_T} = \frac{\rho c^2}{\gamma} \,, \quad \frac{T\beta_p^2}{\rho c_v \chi_T} = \gamma - 1 \text{ and } \quad \frac{\beta_p}{\rho c_v \chi_T} = \frac{\beta_p c^2}{c_p} \,. \tag{A.4}$$

Using relations (A.4) in both equations (A.2) and (A.3), we obtain the equation which express the conservation of energy in terms of pressure variable (8). Note that the introduced equations do not involve any hypothesis about the considered fluid.

Appendix B. Method of Manufactured Solutions

As discussed earlier in Section 5.3, source terms appear from the method of manufactured solution and they are added in the right hand side of all resolved equations. In the case of an anisothermal flow without viscous dissipation rate of energy and not subject to gravity, it is necessary to add three source terms for the resolved momentum, energy and pressure equations as

$$\dot{S}_{\boldsymbol{v}} = \rho \frac{D\boldsymbol{v}}{Dt} + \boldsymbol{\nabla} p - \boldsymbol{\nabla} \cdot (\mu \dot{\boldsymbol{\gamma}}) + \frac{2}{3} \boldsymbol{\nabla} \left(\mu \boldsymbol{\nabla} \cdot \boldsymbol{v} \right) \,, \tag{B.1a}$$

$$\dot{S}_e = \rho c_p \frac{DT}{Dt} - T \beta_p \left(\frac{\partial p}{\partial t} + \boldsymbol{v} \cdot \boldsymbol{\nabla} p \right) - \boldsymbol{\nabla} \cdot (\lambda \boldsymbol{\nabla} T) \,, \tag{B.1b}$$

$$\dot{S}_p = \frac{Dp}{Dt} + \rho c^2 \boldsymbol{\nabla} \cdot \boldsymbol{v} - \left(\frac{\beta_p c^2}{c_p} \right) \left(\boldsymbol{\nabla} \cdot (\lambda \boldsymbol{\nabla} T) + \dot{S}_e \right) \,. \tag{B.1c}$$

As we do not solve energy considering isothermal flow, we only compute two source terms for momentum and pressure equations. The isothermal pressure source term reads

$$\dot{S}_p = \frac{Dp}{Dt} + \rho c^2 \boldsymbol{\nabla} \cdot \boldsymbol{v} \,. \tag{B.2}$$

As we consider a perfect gas in Section 5.3, the time- and -space-dependent thermodynamic properties of the fluid are computed as $\rho = p/RT$, $\chi_T = 1/p$, $\beta_p = 1/T$ and $c^2 = \gamma p/\rho$.

For the sake of reproducibility, the source terms of the isothermal manufactured solution (see Section 5.3.1) is given below. They are the result of the differentiation of equations (B.1a) and (B.2) The momentum and pressure source terms read respectively

$$\begin{aligned}
\dot{S}_{\boldsymbol{v}_x} = & 4\pi^2 \mu u_0 \cos(2\pi f t) \; \big\{ \sin^2(\pi x) \sin(2\pi y) - \sin(2\pi y) \cos^2(\pi x) \\
& \qquad + \sin^2(\pi x) \sin(2\pi y) - \sin(\pi y) \cos(2\pi x) \cos(\pi y) \big\} \\
& + \frac{2\mu}{3} u_0 \cos(2\pi f t) \left\{ 2\pi^2 \sin(2\pi y) \cos^2(\pi x) - 2\pi^2 \sin^2(\pi x) \sin(2\pi y) \right. \\
& \qquad \left. + 4\pi^2 \sin(\pi y) \cos(2\pi x) \cos(\pi y) \right\} \\
& + p_1 \pi \cos(2\pi f t) \quad \cos(\pi x) \sin(\pi y) \\
& + 2\pi u_0 \frac{p(x,y,t)}{T_0 R} \quad \big\{ -f \sin^2(\pi x) \sin(2\pi y) \sin(2\pi f t) \\
& \qquad + u_0 \sin^3(\pi x) \sin^2(2\pi y) \cos(\pi x) \cos^2(2\pi f t) \\
& \qquad + u_0 \sin^2(\pi x) \sin(2\pi x) \sin^2(\pi y) \cos(2\pi y) \cos^2(2\pi f t) \big\}
\end{aligned} \tag{B.3}$$

$$\begin{aligned}
\dot{S}_{\boldsymbol{v}_y} = & 4\pi^2 \mu u_0 \cos(2\pi f t) \; \big\{ \sin(2\pi x) \sin^2(\pi y) - \sin(2\pi x) \cos^2(\pi y) \\
& \qquad - \sin(\pi x) \cos(\pi x) \cos(2\pi y) + \sin(2\pi x) \sin^2(\pi y) \big\} \\
& + \frac{2\mu}{3} u_0 \cos(2\pi f t) \left\{ 2\pi^2 \sin(2\pi x) \cos^2(\pi y) - 2\pi^2 \sin(2\pi x) \sin^2(\pi y) \right. \\
& \qquad \left. + 4\pi^2 \sin(\pi x) \cos(\pi x) \cos(2\pi y) \right\} \\
& + p_1 \pi \cos(2\pi f t) \quad \cos(\pi y) \sin(\pi x) \\
& + 2\pi u_0 \frac{p(x,y,t)}{T_0 R} \quad \big\{ -f \sin(2\pi x) \sin^2(\pi y) \sin(2\pi f t) \\
& \qquad + u_0 \sin^3(\pi y) \sin^2(2\pi x) \cos(\pi y) \cos^2(2\pi f t) \\
& \qquad + u_0 \sin^2(\pi x) \sin^2(\pi y) \sin(2\pi y) \cos(2\pi x) \cos^2(2\pi f t) \big\} \,,
\end{aligned} \tag{B.4}$$

$$\begin{aligned}
\dot{S}_p = & \pi p_1 u_0 \cos^2(2\pi f t) \left\{ \sin^2(\pi x) \sin(\pi y) \sin(2\pi y) \cos(\pi x) + \sin(\pi x) \sin(2\pi x) \sin^2(\pi y) \cos(\pi y) \right\} \\
& + \gamma 2\pi u_0 p(x,y,t) \cos(2\pi f t) \left\{ \sin(\pi x) \sin(2\pi y) \cos(\pi x) + \sin(2\pi x) \sin(\pi y) \cos(\pi y) \right\} \\
& - 2\pi f p_1 \sin(\pi x) \sin(\pi y) \sin(2\pi f t) \,.
\end{aligned} \tag{B.5}$$

Sources terms have been computed using the symbolic computing `python` module `sympy`. Due to the long analytical expressions of the source terms for the anisothermal manufactured solution (see Section 5.3.2), we do not include them in the appendix. We refer the reader to the initialization file of each test case available in the `notus` repository [46].

Test-case	T^* in K	μ^* in Pa s	λ^* in W m^{-1} K^{-1}
Le Quéré et al. [15] case T2	273	1.68×10^{-5}	2.38×10^{-2}
Bouafia and Daube [63]	300	1.68×10^{-5}	2.38×10^{-2}
Wen et al. [64]	273	2.96×10^{2}	2.30×10^{-1}

Table C.11: Values of the parameters of the Sutherland law for the proposed test cases. All test cases have the same $S = 110.5$.

Appendix C. Parameter values of material laws

For the sake of easily reproducible verification and validation process, we present in Table C.11 the values of the Sutherland law parameters used in our test cases. We recall the Sutherland law for a material properties x

$$x(T) = x^* \left(\frac{T}{T^*}\right)^{3/2} \frac{T^* + S}{T + S}\,, \tag{C.1}$$

with x^*, T^* and S the three parameters of the law.

The viscosity and conductivity law of the thermoacoustic wave propagation of Huang and Bau [66] has been set by a quartic temperature law polynomial. Material properties x is thus computed as

$$x(T) = \sum_{i=0}^{3} a_{xi} T^i\,, \tag{C.2}$$

with a_{xi} the i^{th} constant parameter in $[x]\mathrm{K}^{-i}$ with $[x]$ the unit of x. We set for viscosity and conductivity respectively

$$(a_{\mu 0}, a_{\mu 1}, a_{\mu 2}, a_{\mu 3}) = (1.24\times10^{-6}, 6.32\times10^{-8}, -4.65\times10^{-11}, 2.01\times10^{-14})\,, \tag{C.3}$$

$$(a_{\lambda 0}, a_{\lambda 1}, a_{\lambda 2}, a_{\lambda 3}) = (-7.26\times10^{-4}, 9.76\times10^{-5}, -7.18\times10^{-8}, 3.10\times10^{-11})\,. \tag{C.4}$$

References

[1] S. K. Godunov and I. O. Bohachevsky. Finite difference method for numerical computation of discontinuous solutions of the equations of fluid dynamics. 1959. URL https://api.semanticscholar.org/CorpusID:126255486.

[2] P.L Roe. Approximate riemann solvers, parameter vectors, and difference schemes. *Journal of Computational Physics*, 43(2):357–372, 1981. ISSN 0021-9991. doi: https://doi.org/10.1016/0021-9991(81)90128-5. URL https://www.sciencedirect.com/science/article/pii/0021999181901285.

[3] R.W. Maccormack. A numerical method for solving the equations of compressible viscous flow. *AIAA Journal*, 20:1275–1281, 1981. URL https://api.semanticscholar.org/CorpusID:209843221.

[4] S. LeMartelot, B. Nkonga, and R. Saurel. Liquid and liquidgas flows at all speeds. *Journal of Computational Physics*, 255:53–82, 2013. ISSN 0021-9991. doi: https://doi.org/10.1016/j.jcp.2013.08.001. URL https://www.sciencedirect.com/science/article/pii/S0021999113005263.

[5] E. Turkel. Preconditioned methods for solving the incompressible and low speed compressible equations. *Journal of Computational Physics*, 72(2):277–298, 1987. doi: https://doi.org/10.1016/0021-9991(87)90084-2.

[6] A. Murrone and H. Guillard. Behavior of upwind scheme in the low mach number limit: Iii. preconditioned dissipation for a five equation two phase model. *Computers & Fluids*, 37:1209–1224, 2008. URL https://api.semanticscholar.org/CorpusID:122921360.

[7] M. Pelanti. Low mach number preconditioning techniques for roe-type and hllc-type methods for a two-phase compressible flow model. *Applied Mathematics and Computation*, 310:112–133, 2017. ISSN 0096-3003. doi: https://doi.org/10.1016/j.amc.2017.04.014. URL https://www.sciencedirect.com/science/article/pii/S0096300317302588.

[8] S. Dellacherie. Analysis of godunov type schemes applied to the compressible euler system at low mach number. *Journal of Computational Physics*, 229(4):978–1016, 2010. ISSN 0021-9991. doi: https://doi.org/10.1016/j.jcp.2009.09.044. URL https://www.sciencedirect.com/science/article/pii/S0021999109005361.

[9] X.S. Li and C.W. Gu. An all-speed roe-type scheme and its asymptotic analysis of low mach number behaviour. *Journal of Computational Physics*, 227(10):5144–5159, 2008. ISSN 0021-9991. doi: https://doi.org/10.1016/j.jcp.2008.01.037. URL https://www.sciencedirect.com/science/article/pii/S0021999108000697.

[10] A. J. Chorin. A numerical method for solving incompressible viscous flow problems. *Journal of Computational Physics*, 2(1):12–26, 1967. doi: 10.1016/0021-9991(67)90037-x.

[11] S.V. Patankar. *Numerical heat transfer and fluid flow*. Series on Computational Methods in Mechanics and Thermal Science. Hemisphere Publishing Corporation (CRC Press, Taylor & Francis Group), 1980. ISBN 978-0891165224. URL http://www.crcpress.com/product/isbn/9780891165224.

[12] R. Peyret and T.D. Taylor. *Computational Methods for Fluid Flow*. Scientific Computation. Springer Berlin Heidelberg, 2012. ISBN 9783642859526. URL https://books.google.fr/books?id=1az7CAAAQBAJ.

[13] S. Paolucci. On the filtering of sound from the navierstokes equations. *NASA STI/Recon Technical Report N*, 83:26036, 1982.

[14] C. Wall, C. D. Pierce, and P. Moin. A semi-implicit method for resolution of acoustic waves in low mach number flows. *Journal of Computational Physics*, 181(2):545563, 2002. ISSN 0021-9991. doi: 10.1006/jcph.2002.7141.

[15] P. Le Quéré, C. Weisman, H. Paillère, J. Vierendeels, E. Dick, R. Becker, M. Braack, and J. Locke. Modelling of natural convection flows with large temperature differences: A benchmark problem for low mach number solvers. part 1. reference solutions. *ESAIM: Mathematical Modelling and Numerical Analysis*, 39(3):609–616, 2005. doi: 10.1051/m2an:2005027.

[16] V. Daru, P. Le Quéré, M.-C. Duluc, and O. Le Maître. A numerical method for the simulation of low mach number liquidgas flows. *Journal of Computational Physics*, 229(23):8844–8867, 2010. doi: https://doi.org/10.1016/j.jcp.2010.08.013.

[17] A. Bermúdez, S. Busto, M. Dumbser, J.L. Ferrín, L. Saavedra, and M.E. Vázquez-Cendón. A staggered semi-implicit hybrid fv/fe projection method for weakly compressible flows. *Journal of Computational Physics*, 421:109743, 2020. ISSN 0021-9991. doi: https://doi.org/10.1016/j.jcp.2020.109743.

[18] A. Hennink, M. Tiberga, and D. Lathouwers. A pressure-based solver for low-mach number flow using a discontinuous galerkin method. *Journal of Computational Physics*, 425:109877, 2021. ISSN 0021-9991. doi: 10.1016/j.jcp.2020.109877. URL http://dx.doi.org/10.1016/j.jcp.2020.109877.

[19] Y. Cang and L. Wang. An improved fractional-step method on co-located unstructured meshes for weakly compressible flow simulations. *Computers and Fluids*, 253, 2023. doi: 10.1016/j.compfluid.2022.105775.

[20] T. Yabe and P.Y. Wang. Unified numerical procedure for compressibleand incompressible fluid. *Journal of the Physical Society of Japan*, 60(7):2105–2108, 1991. doi: 10.1143/JPSJ.60.2105. URL https://doi.org/10.1143/JPSJ.60.2105.

[21] I. Demirdi, . Lilek, and M. Peri. A collocated finite volume method for predicting flows at all speeds. *International Journal for Numerical Methods in Fluids*, 16(12):1029–1050, 1993. doi: https://doi.org/10.1002/fld.1650161202. URL https://onlinelibrary.wiley.com/doi/abs/10.1002/fld.1650161202.

[22] H. Bijl and P. Wesseling. A unified method for computing incompressible and compressible flows in boundary-fitted coordinates. *Journal of Computational Physics*, 141(2):153–173, 1998. ISSN 0021-9991. doi: https://doi.org/10.1006/jcph.1998.5914.

[23] F. Moukalled and M. Darwish. A unified formulation of the segregated class of algorithms for fluid flow at all speeds. *Numerical Heat Transfer, Part B: Fundamentals*, 37(1):103–139, 2000. doi: 10.1080/104077900275576.

[24] F. Xiao. Unified formulation for compressible and incompressible flows by using multi-integrated moments i: one-dimensional inviscid compressible flow. *Journal of Computational Physics*, 195 (2):629–654, 2004. ISSN 0021-9991. doi: https://doi.org/10.1016/j.jcp.2003.10.014.

[25] F. Xiao, R. Akoh, and S. Ii. Unified formulation for compressible and incompressible flows by using multi-integrated moments ii: Multi-dimensional version for compressible and incompressible flows. *Journal of Computational Physics*, 213(1):31–56, 2006. ISSN 0021-9991. doi: https://doi.org/10.1016/j.jcp.2005.08.002.

[26] D. Fuster and S. Popinet. An all-mach method for the simulation of bubble dynamics problems in the presence of surface tension. *Journal of Computational Physics*, 374:752–768, 2018. doi: https://doi.org/10.1016/j.jcp.2018.07.055.

[27] K. Goda. A multistep technique with implicit difference schemes for calculating two- or three-dimensional cavity flows. *Journal of Computational Physics*, 30(1):76–95, 1979. doi: 10.1016/0021-9991(79)90088-3.

[28] L. J. P. Timmermans, P. D. Minev, and F. N. Van de Vosse. An approximate projection scheme for incompressible flow using spectral elements. *International Journal for Numerical Methods in Fluids*, 22(7):673–688, 1996. doi: 10.1002/(sici)1097-0363(19960415)22:7<673::aid-fld373>3.0.co;2-o.

[29] J.L. Guermond, P. Minev, and Jie Shen. An overview of projection methods for incompressible flows. *Computer Methods in Applied Mechanics and Engineering*, 195(44-47):6011–6045, 2006. doi: 10.1016/j.cma.2005.10.010.

[30] N. Kwatra, J. Su, J.T. Grétarsson, and R. Fedkiw. A method for avoiding the acoustic time step restriction in compressible flow. *Journal of Computational Physics*, 228(11):4146–4161, 2009. ISSN 0021-9991. doi: https://doi.org/10.1016/j.jcp.2009.02.027. URL https://www.sciencedirect.com/science/article/pii/S0021999109000977.

[31] J. M. Vedovoto, A. da Silveira Neto, A. Mura, and L. F. Figueira da Silva. Application of the method of manufactured solutions to the verification of a pressure-based finite-volume numerical scheme. *Computers & Fluids*, 51(1):85–99, 2011. ISSN 0045-7930. doi: https://doi.org/10.1016/j.compfluid.2011.07.014.

[32] G. Huber, S. Tanguy, J.C. Béra, and B. Gilles. A time splitting projection scheme for compressible two-phase flows. application to the interaction of bubbles with ultrasound waves. *Journal of Computational Physics*, 302:439–468, 2015. doi: 10.1016/j.jcp.2015.09.019.

[33] A. Urbano, M. Bibal, and S. Tanguy. A semi implicit compressible solver for two-phase flows of real fluids. *Journal of Computational Physics*, 456:111034, 2022. doi: 10.1016/j.jcp.2022.111034.

[34] A.D. Demou, N. Scapin, M. Pelanti, and L. Brandt. A pressure-based diffuse interface method for low-mach multiphase flows with mass transfer. *Journal of Computational Physics*, 448:110730, 2022. doi: https://doi.org/10.1016/j.jcp.2021.110730.

[35] V. Moureau, C. Bérat, and H. Pitsch. An efficient semi-implicit compressible solver for large-eddy simulations. *Journal of Computational Physics*, 226(2):1256–1270, 2007. ISSN 0021-9991. doi: https://doi.org/10.1016/j.jcp.2007.05.035.

[36] C. J. Roy, C. C. Nelson, T. M. Smith, and C. C. Ober. Verification of Euler/Navier–Stokes codes using the method of manufactured solutions. *International Journal for Numerical Methods in Fluids*, 44(6):599–620, February 2004. doi: 10.1002/fld.660.

[37] C. Bayona, J. Baiges, and R. Codina. Solution of low mach number aeroacoustic flows using a variational multi-scale finite element formulation of the compressible navier–stokes equations written in primitive variables. *Computer Methods in Applied Mechanics and Engineering*, 344: 1073–1103, 2019. doi: 10.1016/j.cma.2018.01.040.

[38] F. Navah. *Development, Verification and Validation of High-Order Methods for the Simulation of Turbulence*. Phd thesis, McGill University, 2019.

[39] J. Muralha, L. Eça, and C.M. Klaij. Code Verification of a Pressure-Based Solver for Subsonic Compressible Flows. *Journal of Verification, Validation and Uncertainty Quantification*, 5(4): 041001, 2020. ISSN 2377-2158. doi: 10.1115/1.4048750.

[40] A. Toutant. General and exact pressure evolution equation. *Physics Letters A*, 381(44):3739–3742, nov 2017. doi: 10.1016/j.physleta.2017.10.008.

[41] S. Y. Yoon and T. Yabe. The unified simulation for incompressible and compressible flow by the predictor-corrector scheme based on the CIP method. *Computer Physics Communications*, 119 (2-3):149–158, 1999. doi: 10.1016/s0010-4655(99)00192-7.

[42] J.-P. Caltagirone, S. Vincent, and C. Caruyer. A multiphase compressible model for the simulation of multiphase flows. *Computers & Fluids*, 50(1):24–34, 2011. doi: 10.1016/j.compfluid.2011.06.011.

[43] H. Terashima and M. Koshi. Approach for simulating gas–liquid-like flows under supercritical pressures using a high-order central differencing scheme. *Journal of Computational Physics*, 231 (20):6907–6923, 2012. doi: 10.1016/j.jcp.2012.06.021.

[44] S. Amiroudine, J.-P. Caltagirone, and A. Erriguible. A lagrangianeulerian compressible model for the trans-critical path of near-critical fluids. *International Journal of Multiphase Flow*, 59:15–23, 2014. doi: doi.org/10.1016/j.ijmultiphaseflow.2013.10.008.

[45] Y. Saade, D. Lohse, and D. Fuster. A multigrid solver for the coupled pressure-temperature equations in an all-mach solver with VoF. *Journal of Computational Physics*, 476:111865, 2023. doi: 10.1016/j.jcp.2022.111865.

[46] Notus computational fluid dynamics, v0.6.0. [https://notus-cfd.org/], 2024.

[47] S. Glockner, A. M. D. Jost, and A. Erriguible. Advanced petascale simulations of the scaling up of mixing limited flow processes for materials synthesis. *Chemical Engineering Journal*, 431(Part 1):133647 (9 p.), 2022. doi: 10.1016/j.cej.2021.133647.

[48] A.H. Baker, R.D. Falgout, T.V. Kolev, and U.M. Yang. *Scaling Hypre's Multigrid Solvers to 100,000 Cores*, pages 261–279. 2012. doi: 10.1007/978-1-4471-2437-5_13.

[49] P. R. Amestoy, I.S. Duff, and J.Y. LExcellent. Multifrontal parallel distributed symmetric and unsymmetric solvers. *Computer Methods in Applied Mechanics and Engineering*, 184:501–520, 2000.

[50] D. Sharma, M. Coquerelle, A. Erriguible, and S. Amiroudine. Adaptive interface thickness based mobilityphase-field method for incompressible fluids. *International Journal of Multiphase Flow*, 142:103687, 2021. doi: 10.1016/j.ijmultiphaseflow.2021.103687.

[51] A.M.D. Jost and S. Glockner. Direct forcing immersed boundary methods: Improvements to the ghost-cell method. *Journal of Computational Physics*, 438:110371, 2021. ISSN 0021-9991. doi: https://doi.org/10.1016/j.jcp.2021.110371.

[52] A.M.D. Jost, S. Glockner, and A. Erriguible. Direct numerical simulations of fluids mixing above mixture critical point. *The Journal of Supercritical Fluids*, 165:104939, 2020. ISSN 0896-8446. doi: https://doi.org/10.1016/j.supflu.2020.104939. URL https://www.sciencedirect.com/science/article/pii/S089684462030190X.

[53] A. Lemoine, S. Glockner, and J. Breil. Moment-of-fluid analytic reconstruction on 2d cartesian grids. *Journal of Computational Physics*, 328:131–139, 2017. doi: https://doi.org/10.1016/j.jcp.2016.10.013.

[54] M. Coquerelle and S. Glockner. A fourth-order accurate curvature computation in a level set framework for two-phase flows subjected to surface tension forces. *Journal of Computational Physics*, 305:838876, 2016. doi: 10.1016/j.jcp.2015.11.014.

[55] W. Oberkampf and T. Trucano. *Verification and Validation in Computational Fluid Dynamics*. 2002. doi: 10.2172/793406.

[56] C. J. Roy. Review of code and solution verification procedures for computational simulation. *Journal of Computational Physics*, 205(1):131156, 2005. doi: 10.1016/j.jcp.2004.10.036.

[57] P.J. Roache. *Verification and Validation in Computational Science and Engineering*. Hermosa Publishers, 1998. ISBN 9780913478080. URL https://books.google.fr/books?id=ENRlQgAACAAJ.

[58] J.-P. Caltagirone. An alternative model of euler equations based on conservation of acceleration. *Submited to Journal of Computational Physics*, 2024.

[59] L. Shunn, F. Ham, P. Knupp, and P. Moin. Verification of low-mach number combustion codes using the method of manufactured solutions. *CSRI Summer Proceedings*, pages 126–36, 2007.

[60] P. Le Quéré. Accurate solutions to the square thermally driven cavity at high rayleigh number. *Computers & Fluids*, 20(1):29–41, 1991. ISSN 0045-7930. doi: 10.1016/0045-7930(91)90025-d.

[61] J. Vierendeels, B. Merci, and E. Dick. Benchmark solutions for the natural convective heat transfer problem in a square cavity with large horizontal temperature differences. *International Journal of Numerical Methods for Heat & Fluid Flow*, 13(8):10571078, 2003. ISSN 0961-5539. doi: 10.1108/09615530310501957.

[62] T. W. I. Kuan and J. Szmelter. A numerical framework for low-speed flows with large thermal variations. *Computers & Fluids*, 265:105989, 2023. ISSN 0045-7930. doi: https://doi.org/10.1016/j.compfluid.2023.105989.

[63] M. Bouafia and O. Daube. Natural convection for large temperature gradients around a square solid body within a rectangular cavity. *International Journal of Heat and Mass Transfer*, 50 (17–18):3599–3615, 2007. doi: 10.1016/j.ijheatmasstransfer.2006.05.013.

[64] X. Wen, L.-P. Wang, and Z. Guo. Development of unsteady natural convection in a square cavity under large temperature difference. *Physics of Fluids*, 33(8), 2021. doi: 10.1063/5.0058399.

[65] K. Khadra, P. Angot, S. Parneix, and J.-P. Caltagirone. Fictitious domain approach for numerical modelling of navierstokes equations. *International Journal for Numerical Methods in Fluids*, 34 (8):651–684, 2000.

[66] Y. Huang and H. H. Bau. Thermoacoustic waves in a confined medium. *International Journal of Heat and Mass Transfer*, 40(2):407419, 1997. doi: 10.1016/0017-9310(96)00068-3.

[67] B. Farouk, E. S. Oran, and T. Fusegi. Numerical study of thermoacoustic waves in an enclosure. *Physics of Fluids*, 12(5):10521061, 2000. doi: 10.1063/1.870360.

[68] Y. Miura, S. Yoshihara, M. Ohnishi, K. Honda, M. Matsumoto, J. Kawai, M. Ishikawa, H. Kobayashi, and A. Onuki. High-speed observation of the piston effect near the gas-liquid critical point. *Physical Review E*, 74(1), 2006. doi: 10.1103/physreve.74.010101.

[69] P. Zhang and B. Shen. Thermoacoustic wave propagation and reflection near the liquid-gas critical point. *Physical Review E*, 79(6), 2009. doi: 10.1103/physreve.79.060103.

[70] P. Carlès. Thermoacoustic waves near the liquid-vapor critical point. *Physics of Fluids*, 18(12), 2006. doi: 10.1063/1.2397577.

[71] A. Poux, S. Glockner, and M. Azaïez. Improvements on open and traction boundary conditions for navierstokes time-splitting methods. *Journal of Computational Physics*, 230(10):4011–4027, 2011. ISSN 0021-9991. doi: https://doi.org/10.1016/j.jcp.2011.02.024.

[72] C. Bozonnet, O. Desjardins, and G. Balarac. Traction open boundary condition for incompressible, turbulent, single- or multi-phase flows, and surface wave simulations. *Journal of Computational Physics*, 443:110528, 2021. ISSN 0021-9991. doi: https://doi.org/10.1016/j.jcp.2021.110528. URL https://www.sciencedirect.com/science/article/pii/S002199912100423X.